UCLouvain

École polytechnique de Louvain

Analytical model calibration and axial induction power optimization for three wind turbines in a row

Authors : **Bruno Cheppe, Aurélien Philipin**
Supervisors **: Philippe Chatelain, Matthieu Duponcheel, Grégoire Winckelmans**
Reader : **Yann Bartosiewicz**
Academic year 2021–2022
Master [120] in Electro-mechanical Engineering, Master [120] in Mechanical Engineering

Aknowledgements / Remerciements

En premier lieu, nous tenons à remercier nos trois promoteurs : le professeur Philippe Chatelain, le docteur Matthieu Duponcheel, le professeur Grégoire Winckelmans, mais aussi les autres membres du TFL pour le suivi durant l'année et leurs présences aux réunions. Il était important pour nous de pouvoir bénéficier de leurs conseils et de la maîtrise qu'ils ont du sujet pour pouvoir avancer dans notre travail. Un merci tout particulier au professeur Philippe Chatelain pour sa relecture et les conseils dont il nous a fait part pour améliorer le fond et la forme de ce manuscrit.

Nous tenons également à remercier Maxime Lejeune et François Trigaux, pour le soutien qu'ils nous ont apporté tout au long de l'année. Leurs disponibilités, conseils, et leur maîtrise du sujet nous ont épaulés durant toute l'année et nous ont permis d'avancer pour atteindre l'objectif. Finalement, nous tenons à les remercier pour les nombreuses relectures et leurs avis pertinents concernant l'écrit.

On remercie également le professeur Yann Bartosiewicz d'avoir accepté d'être membre du jury pour la défense ainsi que la lecture de notre mémoire.

Pour la relecture, nous tenons également à remercier Alexandra Charlier, Eléonore Lieffrig, Manuel Pace et Muhammad Usama Bin Shehzad. Leur regard extérieur, leur maîtrise de l'anglais, et leurs avis sur le fond et la forme ont permis d'améliorer ce travail.

Finalement, nous voulons remercier nos familles respectives, nos amis, Mercataule, Constanteuf, l'ADELE et nos concubines Alexandra Charlier et Alizée Hector pour leurs présences et leurs soutiens durant les années à l'EPL.

Abstract.

The most common techniques used by the wind energy sector to forecast the power output of wind farms are analytical wake models and wake superposition models. However, a sufficiently accurate model for the axial-induction-based control for three wind turbines in a row spaced of seven rotor diameters apart can not be developed based on the literature. Therefore, the investigation and calibration of the farm's wake model take up a significant portion of the work.
The focus of the second part of this document is on the axial-induction-based wind plant control methods using our pre-calibrated farm model. This power optimization method allows wind turbines degrees of freedom to be changed by adjusting their rotor speed or blade pitch. However, most of the time, wind turbines are operated to their maximum potential without considering the impacts of the wake on nearby wind turbines. Through the coordination of the turbines' operations, wind plant control seeks to improve the overall performance of the wind farm.

Contents

Chapter 1

Introduction

1.1 Context and state of the art

Nowadays, global warming is a major concern. The main issue is to limit the production of greenhouse gases and CO_2. These gases are responsible for the progressive increase of the average global temperature and all the consequences that this implies. Indeed, greenhouse gases trap heat and make the planet warmer [3]. The increase in greenhouse gases is linked to a grow up of human activities over the last 150 years. In 2020, 73.2% of these greenhouse gases were released due to energy production [19]. It is the sector of activity that produces the most greenhouse gases. This is mainly due to the burning of fossil fuel. This refers to the burning of oil, natural gas, and coal to generate energy. After that, we exploit this energy to generate electricity and to power transformation [2]. To overcome these issues, we must develop other kinds of electricity production, such as wind turbines and solar panels.

We will focus on wind energy. This source of energy allows several advantages [1]. First of all, it is a clean fuel source. Unlike power plants that rely on the combustion of fossil fuel, which emits particulate matter, wind turbine energy does not pollute the air. Secondly, this one is sustainable and inexhaustible. Indeed, the wind on which they depend comes from the heating of the atmosphere by the sun. As long as the sun shines, there will be wind. The trouble spot is that turbines can create noise with the rotation of the blades and aesthetic pollution on the landscape. To minimize these nuisances, the solution is to group several wind turbines on a land relatively far from civilization. We call it a wind farm.

Figure 1.1: Photo by Christian Steiness / Vattenfall (Horns Rev Offshore Wind Farm, Denmark). Original Image Link: http://i.imgur.com/qruVcnu.jpg

However, in order to produce a maximum power and make the best use of the space, it is important to place the right amount of wind turbines at the right places. The goal is to reduce the effect of interactions between different wind turbines while making the most of the space. In fact, when the wind turbines are aligned with the wind direction, the wakes of the first turbines enter the downstream ones. This results in power losses in the downstream turbines and has a strong impact on the total power of the farm. There are different ways to reduce the impact of upstream wind turbines on downstream ones. The turbines can rotate (by a yaw angle) to get out of alignment with the wind and have their wakes deviate from the downstream turbines. We can also accept to decrease the rotational speed or increase the angle of inclination of the blade (called pitch angle) of a wind turbine creating a low-power loss in order to reduce the wakes perceived by the downstream. Our analysis will focus on this rotor speed and pitch angle variation.

To model a wind farm, several numerical approaches are used, according to their level of fidelity. The first approach is the analytical model, the so-called "wake model". These are time-averaged models that allow predicting the development of the wake, under steady conditions, with low fidelity. Many studies are carried out using this method because of their benefit of having a short runtime, and are therefore very efficient. To predict the wake, this approach uses the conservation of mass and momentum equations for an established control volume, and the momentum theory. A pioneer of these analytical wake models is Jensen [12], who assumes a top-hat model for the velocity deficit in the wake. This last is for example used by commercial software such as WaSP or WindPro [21]. Other wake models have been developed, assuming that the wake deficit (time-averaged) is a Gaussian function. Bastankhah and Porté-Agel use this approach to predict the wake [15]. The results of this first approach are compared and validated against the high-fidelity method using Computational Fluid Dynamics (CFD). To perform simulations, the most commonly used technique is Large Eddy Simulation (LES). This technique allows to obtain a more accurate wake behaviour and to capture unsteady effects, with acceptable computational costs. To perform wake simulations, we need to combine LES and the modelling of the wind turbine through an Actuator Disk (AD).

1.2 Objectives of the thesis

The objectives of this thesis are therefore to study the power of a farm composed of 3 wind turbines spaced far of 7 rotor diameters in a row to maximize it. This optimization is done by modifying the pitch angle and the rotational speed of the blades. The NREL-5MW reference wind turbine is here considered [11].

To perform the optimization, it is important to correctly calibrate the wake model on an isolated wind turbine. Indeed, we have to adjust the analytical wake model according to the expansion factor (see later: section 2.1.1). For calibration purposes, we have to compare our results with the BigFlow solver (explained in section: 2.3). After that, the impact of the model parameters on the wakes are studied (section: 3.2). Then, we have tried to see if it was possible to have an outflow wind at 7D (the place of the next turbine) which is close to the one of BigFlow trough a wake model, with a shape corresponding to reality (section: 3.3). Later, the impact of the operating points and conditions on the expansion factor are studied to find a way to compute the expansion factor without having to calibrate it (section: 3.4.1). Once the model is calibrated, a wake superposition model is used to extend the model found for one wind turbine to a farm of 3 wind turbines (section: 3.5). Finally, the model is exploited to compute and optimize the power of the farm by varying the pitch angle and the rotor speed (section: 4). Before doing all this, it is important to develop in more detail the tools and methodology that are needed (section: 2). Indeed, we develop the analytical wake model, the superposition wake models and the solver BigFlow (section: 2.1, 2.1.2, 2.3) and the other necessary tools needed (section: 2.2 to 2.5).

Chapter 2

Methodology

In this chapter, we theoretically present the wake and superposition models that will be used for our farm. We introduce the BigFlow solver that will be our point of comparison for the wakes. To finally understand the model assembly of the farm, the Blade Element Momentum (BEM) operation and how we find the wind turbine rotational speed and the pitch angle (useful for calibration) are explained.

2.1 Analytical wake models

Wind farms power production is known to be strongly impacted by turbine wake effects. Therefore, it is important to accurately predict the wake flow. To do so, a lot of research has been done and has led to the creation of wake prediction models. The development of these models consists in applying conservation equations to develop an analytical equation. It represents the wake created by a wind turbine, depending on its operating parameters such as the thrust coefficient. The set of these equations is called an analytical wake model. Note that these models do not return instantaneous wake, but the output of the model is a time-averaged wake. Now, one can look at the development of a wake model often used in the literature.

2.1.1 Isolated wind turbines

M. Batstankhah & F. Porté-Agel model

Among the analytical wake models for isolated wind turbines, M. Batstankhah & F. Porté-Agel have developed a model which is commonly adopted in the literature [15]. As already mentioned, the velocity deficit downstream of a wind turbine strongly looks like a Gaussian profile for time-averaged wake in the streamwise direction with the wind aligned with the rotor. Bastankhah and F. Porté-Agel developed a Gaussian model, by applying mass and momentum conservation. They assumed a Gaussian wake shape function of the form :

$$\frac{\Delta U}{U_\infty} = C(x) \cdot \exp\left(\frac{-r^2}{2\sigma^2(x)}\right) \tag{2.1}$$

Where:

- $C(x)$ is the maximum normalized velocity deficit at each downwind position x, at the centre of the wake.
- The speed deficit ΔU is the difference between the freestream velocity and the wake velocity: $\Delta U = U_\infty - u_w$.
- r is the radial distance from the centre of the wake.
- $\sigma(x)$ is the standard deviation of the Gaussian profile for the velocity deficit.

The momentum conservation is then applied (Eq. 2.2) in order to derive an expression for $C(x)$ and $\sigma(x)$:

$$\rho \int u_w(U_\infty - u_w)dA = T \tag{2.2}$$

$$C_T = \frac{T}{0.5\rho U_\infty^2 A} \tag{2.3}$$

Where:

- T is the force thrust over the wind turbine
- ρ is the air density
- A is the area covered by the disk formed by the blades.
- C_T is the thrust coefficient

Where Eq. 2.3 is the definition of the thrust coefficient C_T. This last is the first parameter of the model. Then, Eq. 2.1 can be rearranged :

$$u_w = U_\infty(1 - C(x)e^{\frac{-r^2}{2\sigma^2(x)}}) \tag{2.4}$$

Substituting this relation, and relation 2.3 into the momentum equation (Eq. 2.2) and integrating from 0 to ∞, it turned out to be :

$$8\left(\frac{\sigma(x)}{D}\right)^2 C(x)^2 - 16\left(\frac{\sigma(x)}{D^2}\right)^2 C(x) + C_T = 0 \tag{2.5}$$

D being the rotor diameter. N. Jensen, a pioneer in analytical wake models (well known for his top-hap shape model [12]), assumes a linear expansion for the wake region. This linear relation is Eq. 2.6 By doing so Eq. 2.5 can be resolved for $C(x)$, leading to Eq. 2.7

$$\frac{\sigma(x)}{D} = k^* \frac{x}{D} + \epsilon \tag{2.6}$$

$$C(x) = 1 - \sqrt{1 - \frac{C_T}{8\left(\frac{\sigma(x)}{D}\right)^2}} \tag{2.7}$$

Where:

- $k^* = \partial\sigma(x)/\partial x$ is the growth rate of the wake due to turbulent mixing, commonly called expansion coefficient.
- ϵ is the initial standard deviation of the wake (at x = 0, $\epsilon = \epsilon_{(C_T)}$).

The root found for C(x) in the second degree equation is the physically acceptable solution (which predicts correct deficits at larger downwind distances). Thanks to all these variables, the speed deficit, normalized by the freestream velocity can be formulated as:

$$\frac{\Delta U}{U_\infty} = \left(1 - \sqrt{1 - \frac{C_T}{8(\sigma(x)/D)^2}}\right) \times \exp\left(-\frac{1}{2((\sigma(x)/D))^2}\left\{\left(\frac{y}{D}\right)^2 + \left(\frac{z}{D}\right)^2\right\}\right) \tag{2.8}$$

C. Shapiro *et al.* model

Shapiro *et al. (2018)* ([23]) reformulated Eq. 2.8 by isolating $u_w(x,y,z)$, for modelling yawed wind turbines. In this section, we explain the different hypothesis and derive elements such as $\sigma(x)$, $\delta u(x)$ (the axial velocity deficit) which are defined differently from the previous section. In this research and for the further model simulations, we will use this equation, without considering yaw angle - without taking into account the transverse velocity, which gives :

$$u(x,y,z) = U_\infty - \delta u(x) \cdot \frac{D^2}{8\sigma_0^2} \times \exp\left(-\frac{y^2+z^2}{2\sigma^2(x)}\right) \tag{2.9}$$

$$A(x) = d_w^2(x)\pi D^2/4 \tag{2.10}$$

This function written by Shapiro *et al.* (Eq. 2.9) is taken from the work of Bastankah *et al.* They assume, as Bastankhah did, that the effective area (Eq. 2.10) is only function of x, since the wake expands due to turbulent mixing. However, this area depends on the effective diameter d_w. Thus, the expansion wake region is no longer considered as a function linear to x, but this diameter is related to the equation :

$$d_w(x) = 1 + k^* \ln\left[1 + \exp\left(\frac{x - 2\Delta_w}{R}\right)\right] \tag{2.11}$$

$$\sigma(x) = \sigma_0 \cdot d_w(x) \tag{2.12}$$

The advantage of using this equation is that the flow will start to expand at $x \cong 2\Delta_w$, with characteristic width $\Delta_w = R$. As we will see below, an inviscid region near the rotor is considered in this approach, that is the reason why the expansion starts further. Furthermore, d_w will always stay above 1 and so, the width of the Gaussian in x = 0 is fixed: $\sigma_0 = 0.235$. These benefits can be seen in Fig. 2.1.

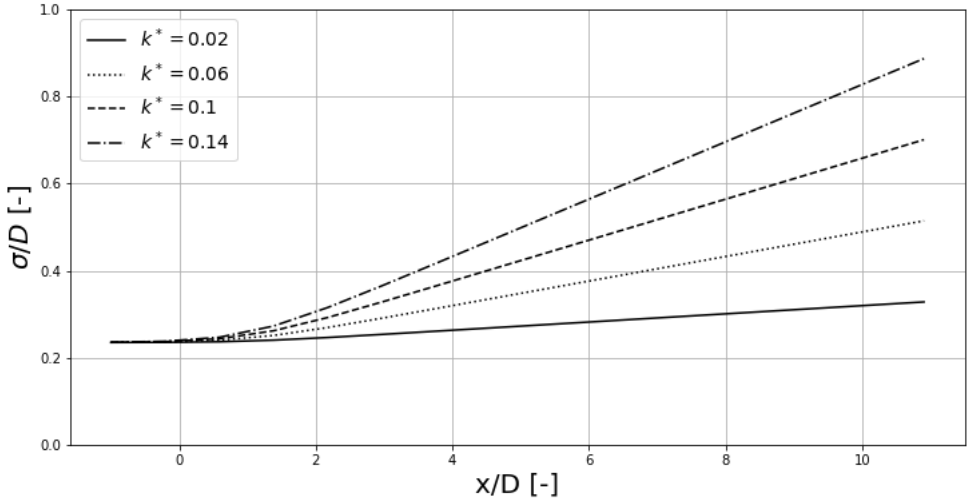

Figure 2.1: Normalized standard deviation of the velocity deficit profiles for different expansion coefficients k^*.

Fig. 2.1 shows the width growth rate for different expansion coefficients. A bigger value of k^* make a larger wake width growth, allowing the flow to recover faster. In this regard, studies on the expansion coefficient have been made in section 3.2.
An expression for the speed deficit, $\delta u(x)$, is finally obtained using the momentum equation (Eq. 2.13), neglecting the viscous terms and linearizing the advective term. The Reynolds stress tensor

is not directly taken into account, but effects of turbulence are modeled by the wake expansion rate : $w(x) = U_\infty A^{-1} dA(x)/dx$. All these elements are substituted in the momentum equation :

$$\frac{\partial \delta u_i}{\partial t} + U_\infty \frac{\partial \delta u_i}{\partial x} = -w(x)\delta u_i(x,t) + S_i \delta(x) \tag{2.13}$$

Then, since the thrust force and pressure gradient terms are acting on the region near the turbine rotor (considered as inviscid here), they are modelled as a source deficit of momentum **S**. Considering only the streamwise direction, we will stick to the x-component for the source of the deficit ($\mathbf{S} = S_i$). The latter defines δu_0 at the end of the inviscid region. The equation can be rewritten:

$$S_i = U_\infty \cdot \delta u_0 \tag{2.14}$$

$$\delta u_0 = 2aU_\infty \tag{2.15}$$

Shapiro *et al.* use the incompressible momentum theory in the inviscid region, they find a value for the initial axial velocity deficit δu_0, which relates the induction factor to a, which in turn is related to the thrust coefficient in this theory as : $a = 1 - \sqrt{1 - C_T}$

Considering steady-state, and integrating Eq. 2.13 along x, yields :

$$\delta u(x) = \frac{1}{2} \frac{\delta u_0}{d_w^2(x)} \left[1 + erf\left(\frac{x}{\Delta_w \sqrt{2}} \right) \right] \tag{2.16}$$

To link the isolated wind turbine wake model developed to all the farm, the superposition models are needed. These are the subject of the next section.

2.1.2 Wake superposition models

When computing the output of a wind farm (i.e. total mechanical power), it is important to take into account the interactions that the turbines have with each other. Indeed, this study allows placing the turbines, and to give them the operating point in order to establish the wake losses. Then, this model is used in order to optimize the global power of the farm. In this perspective, the superposition models are developed. The closer the superposition model is to reality, the more realistic is the wake flow and thus, the power optimization will be more meaningful.

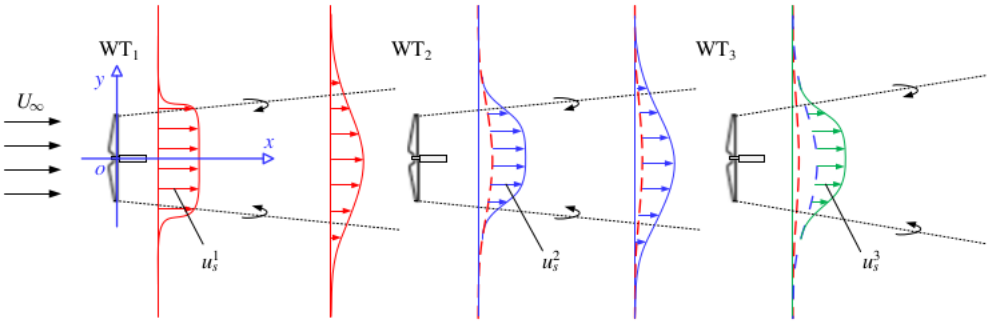

Figure 2.2: Sketch of wake superposition in a three-row wind farm. Here, u_i^s denotes the wake velocity deficit caused by the i^{th} wind turbine (WT_i).[24]

To better understand how superposition of wakes works, Fig. 2.2 shows us that the deficit of each wind turbine effects the downstream one. Therefore, the first wind turbine (deficit in red) has an impact on the two other wind turbines. The velocity at some location x results from the superposition of the speed deficit shed by the wind turbines of the farm.

Zong [24] concluded several empirical relations allowing computing of the δu superposition. These relations are mentioned below:

$$Method\,A : u_w(x,y,z) = U_\infty - \sum_i (U_\infty - u_w^i(x,y,z)) \tag{2.17}$$

$$Method\,B : u_w(x,y,z) = U_\infty - \sqrt{\sum_i (U_\infty - u_w^i(x,y,z))^2} \tag{2.18}$$

$$Method\,C : u_w(x,y,z) = U_\infty - \sum_i (u_{in}^i - u_w^i(x,y,z)) \tag{2.19}$$

$$Method\,D : u_w(x,y,z) = U_\infty - \sqrt{\sum_i (u_{in}^i - u_w^i(x,y,z))^2} \tag{2.20}$$

Where :

- u_{in}^i is the mean wind velocity perceived by the i^{th} wind turbine
- u_w^i is the wake velocity induced by WT_i in stand-alone conditions.
- U_∞ inflow velocity of the wind farm

Method A *(P.B.S. Lissaman [14])* and B *(I. Katic , J. Højstrup , N. O. Jensen [10])* are based on the fact that there is a large spacing between each wind turbine. This means that the mean wind velocity experienced by the downstream turbines can be approximated by the inflow velocity of the wind farms. For the method A, the momentum deficit term can be written as: $(U_\infty\text{-}u_s^i)\cdot u_s^i$ with $u_s^i = u_{in}^i$ - u_w^i which defines the individual wake velocity deficit. This expression can be approximated with $U_\infty \cdot u_s^i$. Thus, we have to sum the wake velocity deficits linearly to conserve the total momentum deficit in the wake. For the method B, the same assumption is conserved (large spacing between each turbine), but in this case, the wake superposition is made by summing the square of the wake velocity deficits. The author expected to conserve the mean kinetic energy deficit during wake interaction. This is disputable because of the not conserved kinetic energy flux in the wake flow due to the turbulent dissipation.

Method C *(A. Niayifar F. Porté-Agel [4])* and D *(S. Voutsinas, K. Rados A. Zervos [20])*, a similar reasoning as for method A and B is used, but the approximation $u_{in}^i \approx U_\infty$ is removed. Instead, the inflow wind is replaced by the mean wind velocity perceived by the i^{th} wind turbine: u_{in}^i determined from the upstream turbine. Thus, wake deficit u_w^i are computed from upstream to downstream turbines. Therefore method C and D are expected to give better predictions of the wind farms' power production particularly when each wind turbine is close to each other.

To work, these models need the thrust coefficient. This one is computed with a blade element momentum.

2.2 Rotor aerodynamics: BEM theory

Blade Element Momentum Theory (BEM) is a combination of two theories: Blade Element Theory (BET) and Momentum Theory (MT). BET consists in splitting the blade into n elements Δr and identify the aerodynamic forces acting on each element, thanks to the local velocities, the lift and drag coefficient of the airfoil.

Wind turbines are represented through an AD in the BigFlow solver, using BET to compute all forces applied to each cell of the AD. It is shown how to obtain the equations for the lift L and drag D, that are further transformed into normal and tangential components, to be applied on each cell of the AD.

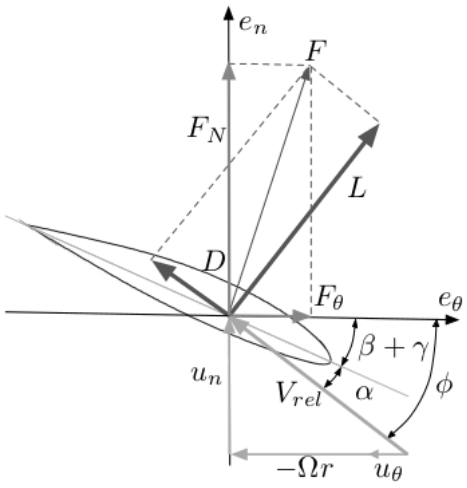

Figure 2.3: Schematics of a blade airfoil, definition of angles and vectors quantities. [17]

The Fig. 2.3 shows the relevant vectors and values for the BEM :

- α : angle of attack
- β : pitch angle
- γ : twist angle
- $\phi = \alpha + \beta + \gamma$: flow angle
- u_n : normal velocity of the incoming wind
- u_θ : tangential velocity of the incoming wind
- Ωr : tangential speed of the rotor at radius r.

The relative velocity V_{rel} and the flow angle are defined :

$$V_{rel} = \sqrt{u_n^2 + (\Omega r - u_\theta)^2} \tag{2.21}$$

$$\phi = \arctan\left(\frac{u_n}{\Omega r - u_\theta}\right) \tag{2.22}$$

The angle of attack is found, thanks to the definition here above $\alpha = \phi - (\beta + \gamma)$. The twist angle γ is a geometric and fixed angle, directly due to the blade twist; the pitch angle β is a control parameter that directly affects the angle of attack. Then, the local lift and drag coefficients can be computed since $C_l, C_d = C_l(\alpha), C_d(\alpha)$. By definition of these coefficients, the lift and drag aerodynamic forces per unit length, applied to each element can be derived :

$$(L, D) = 0.5\rho V_{rel}^2 c\,(C_l, C_d) \tag{2.23}$$

Where c is the chord of the airfoil. It is from these local aerodynamic forces that normal and tangential components are found, in BigFlow solver.

BEM also uses the incompressible momentum theory, which introduces induction factors. a is the axial induction factor and a' is the tangential induction factor, defined as:

$$a = 1 - \frac{u_n}{U_\infty} \quad \text{and} \quad a' = -\omega_0/\Omega \tag{2.24}$$

$\omega_0 = u_\theta / r$ is induced rotational velocity of the flow. The wind velocity components on the Fig. 2.3 can be rewritten in terms of the induction factors as: $u_n = U_\infty \cdot (1 - a)$ and $u_\theta = \omega_0 r = -a'\Omega r$.

In this theory, the velocity at stations directly upstream and downstream the actuator disk is continuous, whereas a pressure drop Δp is observed. By applying conservation of momentum into a streamtube, which conserves the mass flow, a first equation for the thrust is found :

$$T = \dot{m}(u_\infty - u_e) \tag{2.25}$$

u_e is the exit velocity in the far-wake region (in the sense that the exit pressure recovers the freestream pressure in this region - theory assumption), and $\dot{m}$ is the mass flow rate passing through the disk. Another expression for the thrust is developed in this theory : $T = \Delta p \cdot A$; it traduces the fact that the pressure drop is simply the thrust by unit area. Combining them and applying Bernoulli equation leads to Eq. 2.26, a well-known equation of momentum theory :

$$C_T = 4a(1-a) \tag{2.26}$$

The full demonstration of this result is available on [5]. The BEM procedure compares the local thrust obtained via BET (T_{BET}) and via momentum theory (T_{MT}). T_{BET} is the normal component of L and D forces, whereas T_{MT} use the definition of C_T (Eq. 2.3) and the previous result (Eq. 2.26). Since we computed each force L and D per unit length (Eq. 2.23), we can express the infinitesimal form to compute the total thrust:

$$dT_{BET} = B(L\cos\phi + D\sin\phi)dr \tag{2.27}$$

$$dT_{MT} = \frac{1}{2}\rho U_\infty^2 \cdot 4a(1-a) \cdot 2\pi r dr \tag{2.28}$$

With B the number of blades. Since dT_{BET} must be equal to dT_{MT}, the axial induction factor can be isolated from these equations and then computed. In classical BEM, iterations on the induction factor are done until convergence of it. The same reasoning must be done for the tangential induction factor: compare the torque Q from BET and MT, as we do for the thrust.

To compare the superposition and wake models we will use simulations performed by the BigFlow solver. In the next section, we will see what the BigFlow solver is.

2.3 Computational fluid dynamics

Once the model is established, its parameters must be calibrated by fitting high-fidelity data. Having these data allows comparing the wake expansion/recovery, the superposition of the wakes induced by multiple turbines. A common way to proceed to collect the data is to perform Large Eddy Simulations (LES), for different operating settings. To perform LES of wind farm flow, BigFlow solver is used. BigFlow was first introduced by Georges [9] and Bricteux [6], and later, rewritten by Duponcheel [8] to improve it.

The BigFlow code solves the Navier-Stokes equation for incompressible flows (see section 2.1 from [17] for more details) using a fourth order finite difference method. As the Reynolds number encountered in wind farm flows are too large to allow for Direct Numerical Simulation (DNS), we leverage LES. In a few words, LES decreases the total cost of simulations compared of DNS by solving the larger scales of the flow. Thus, a model is used to represent the smaller scale effects on the larger one using a *subgrid-scale* (SGS) model.

Wind turbine is modelled by Actuator Disk (AD). This method essentially averages the forces acting on the blades and distributes them on a disk, the so-called "AD". The latter is discretized according to a polar grid (Fig. 2.4). All the calculations presented in this thesis use data and airfoil geometries from the "NREL offshore 5-MW baseline wind turbine", its technical report is available in [11].

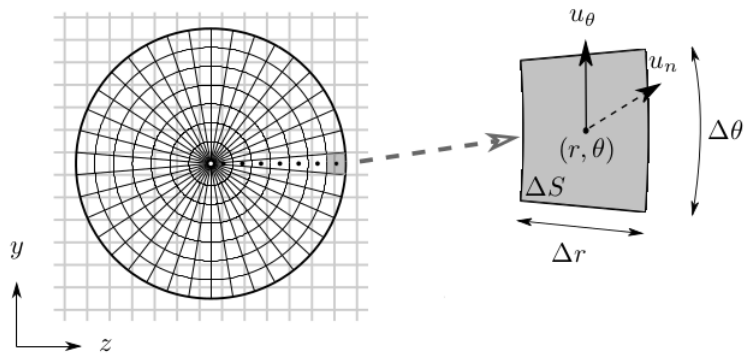

Figure 2.4: Polar mesh used for AD methodology and polar cell in the disk. [17]

Fig. 2.4 represent the AD. On the right side of this figure, a cell at position (r,θ) of area $\Delta S \cong \Delta r \Delta\theta$ is represented. At each time step computation, the forces acting on the cell is equal to the total forces acting on the annular surface, weighted by the area ratio between the surface cell and this annular surface: $\frac{\Delta S}{2\pi r \Delta r}$

These total forces are the aerodynamic forces encountered by the N_b blades in practice. They are calculated using the Blade Element Theory (BET). This technique consists in discretizing the blade into $nElem$ elements of length Δr. Thanks to the characteristics of the airfoil and the local velocities (normal u_n and tangent u_θ), the drag and lift aerodynamic forces are calculated for each blade element. The BET will be seen more in detail in section 2.2.

The characteristics of the wake are strongly influenced by the ambient turbulence. To generate a realistic turbulent inflow, we use Mann's algorithm [16]. The parameters of the inflow can then easily be varied to study the effects of turbulence on the wake, such as the wake recovery. For classical operating conditions, the Turbulence Intensity (TI) of the velocity is about 6 %. TI is defined from the Turbulent Kinetic Energy (TKE) and freestream velocity U_∞. The TKE is the mean kinetic energy per unit mass [J/kg] associated with eddies in turbulent flow.

$$TI = \frac{\sqrt{2/3\,TKE}}{U_\infty} \tag{2.29}$$

$$TKE = \frac{1}{2}(\overline{u'u'} + \overline{v'v'} + \overline{w'w'}) \tag{2.30}$$

Where:

- The overlines denote the time-averaging operator.
- u', v', w' are the velocity fluctuations in $(\hat{e}_x, \hat{e}_y, \hat{e}_z)$ directions.

The simulations are performed into a domain of size $L_x \times L_y \times L_Z = 24D \times 6D \times 6D$, with a resolution of 16 points per diameters (D).

The use of the BEM need operating conditions such as the rotor speed and the pitch angle. The next section present a useful tool to compute the operating parameters.

2.4 Interpolation of pitch angle and rotor speed

In order to predict the wake, the model needs the following operating points : the rotor speed ω and pitch angle β, since the thrust coefficient is a function of them. Therefore, the purpose of this section is to interpolate the operating points coming from BigFlow simulations (performed at several freestream velocity) and thus, obtain a relationship thanks to these interpolated values.

Indeed, when the BigFlow's controller is activated, it adjusts ω and β, depending on the inflow conditions. To keep only a singular ω and β for one BigFlow simulation, the time-averaged values from the temporal BigFlow simulations are used.

Even if later in this document the pitch angle and the rotor speed will vary in order to perform an optimization of the output power, it is still important to know these two variables according to the inflow wind. The correct way to calibrate the model (in particular the expansion coefficient) is to compare wakes performed by the model with those of BigFlow, at fixed operating points for each Wind Turbine (WT). Thanks to this, the results of similar situations can be interpreted. In order to obtain the operating points of BigFlow's turbines, we performed simulations of a wind farm with 3 turbines in a row at different freestream velocities ranging from 8 to 16 [m/s]. By doing so, ω and β for each turbine according to its inflow speed are collected.

The inflow velocity perceived by the first wind turbine equals the freestream velocity, β and ω are gathered according to the freestream velocity (see Fig. 2.5a and Fig. 2.5b). Due to the wake losses, this is no longer the case for the last two wind turbines. Therefore, an inflow velocity for the last two turbines must be found in order to relate the operating points to this waked inflow velocity. This last is computed as the mean wind inflow velocity (i.e. the spatial average on a disk of diameter 1D, centred at the rotor) from BigFlow's simulations.

Since the behaviour of the wind turbines receiving a waked inflow are equivalent, the collected information are combined into one curve (Fig. 2.5a and Fig. 2.5b). Indeed, the behaviour of a wind turbine subjected to a waked inflow is not comparable to the same wind turbine subjected to a non-waked one. This can be seen on the graphs (Fig. 2.5a), the pitch angle value can double at 11 [m/s]. Otherwise, the rotor speed can vary from $\omega \approx 9.75$ to $\omega \approx 10.4$ at 8 [m/s](Fig. 2.5b).

In the chosen range-speed, the rotor speed is capped at 12.1 [rpm], which corresponds to the maximum rotor speed of the NREL 5MW. When the maximum rotor speed of the turbine is reached, and the inflow wind speed continues to increase, the pitch angle is then modified to avoid damage to the wind turbine and to conserve a maximum torque.

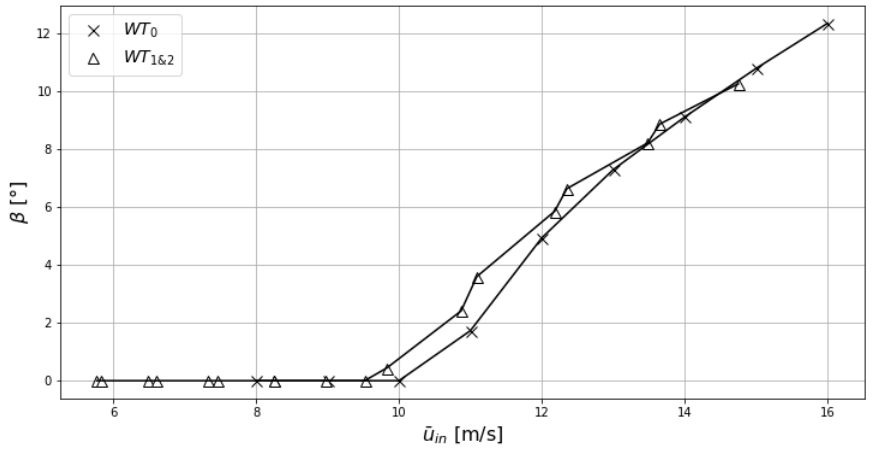

(a)

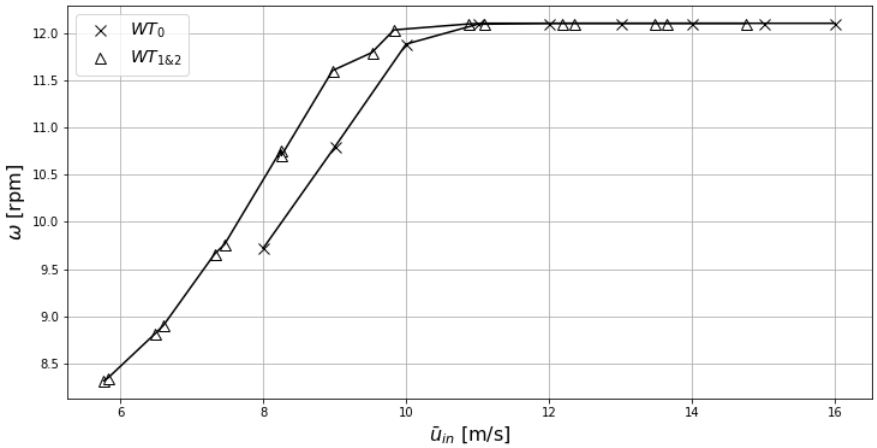

(b)

Figure 2.5: Curve of (a) the pitch (b) rotational speed of the rotor as a function of the wind speed and the character waked or not of the inflow of the WTs.

Knowing the inflow velocity and whether the inflow is waked or not, the operating point of a turbine can be computed thanks to these BigFlow simulations. Now that the model for one wind turbine and the different superposition models have been defined, one can combine these modules, including the interpolation of the operating point, to obtain the final model of the farm.

2.5 Model chain for a wind farm

One can combine the different modules presented above into a block diagram to understand the link between each section to obtain a predictive wake model of our farm.

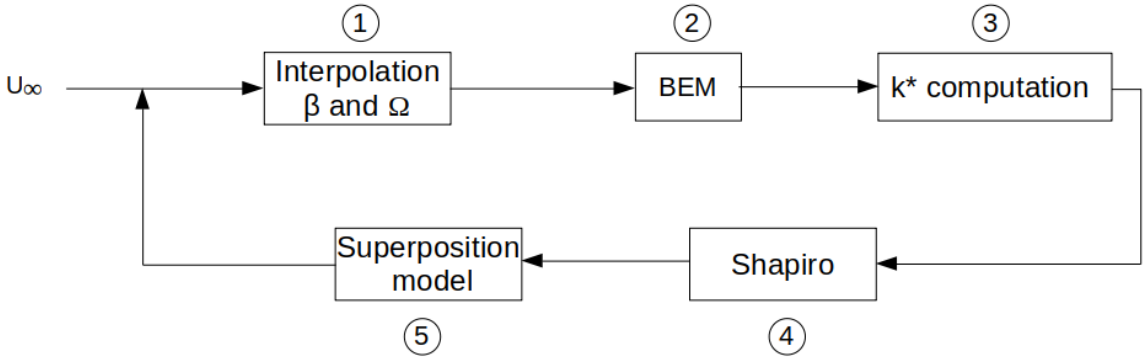

Figure 2.6: Model assembly of the wind farm.

The block diagram in Fig. 2.6 represents the global operation of our system. Each of the blocks, numbered from one to five, will be described in more detail immediately below. It is important to note that the loop described by the diagram is then used three times. The result of each loop gives the induced wake of the corresponding wind turbine, which is then used as the input to compute the next one's wake.

Indeed, we start from the first wind turbine (WT_0) at freestream velocity of the farm: U_∞. After several steps of calculation, we reach the end of step 5. The output of this first loop (of the step 5) is the induced wake by the first wind turbine. A computation of the spatial average wind (called MDV, developed in section 3.1) 7D downstream the WT_0 corresponds to the perceived inflow velocity of the next wind turbine: the input U_∞ becomes u_{in}. In the same way, the loop is executed again to predict the wake of the downstream turbines. To explain the block diagram more in detail, one can start with the first turbine and explain the changes to apply for the others.

1. **Interpolation β and ω**

   Input: U_∞
   Output: β **and** ω**.**

   As explained in Section : 2.4. This block is based on the interpolation of β and ω obtained with BigFlow simulations according to inflow wind. Using this interpolation, β and ω corresponding to U_∞ can be found.

2. **BEM**

   Input: U_∞**,** β**,** ω**.**
   Output: Thrust, Torque
   As explained in Section 2.2, the BEM allows to have the thrust and torque forces as a function of U_∞, ω, and β. This thrust is then used to calculate the thrust coefficient C_T using Eq. 2.3. The torque will be useful for the calculation of the mechanical power and therefore, the optimum output power of the farm.

3. **k^* computation**

   Input: TI**,** U_∞**,** β**,** ω**,** C_T
   Output: k^*
   This block contains several relationships to be able to find the expansion coefficient according to some parameters. Indeed, this parameter k^* will strongly influence the recovery of the wake and so the inflow wind of the next wind turbine. Knowing that later the total power of the farm will be optimized, it is important to have accurate prediction of the outflow for the downstream turbine to have the right optimum.

4. **Shapiro**

   Input: U_∞, C_T, β, λ, k^*
   Output: Wake velocity deficit for one wind turbine

   The Shapiro model is used to predict the speed deficit for the concerned WT, and therefore know the inflow conditions that will reach the next WT. It is important to have accurate input values to perform accurate velocity deficit prediction. This is the reason why the previous blocks were important for the implementation of the Shapiro model. This model works in stand-alone conditions.

5. **Superposition model**

   The model does not go through this block for the first wind turbine.

So finally, the wake of the first WT is obtained. This outflow becomes the inflow for the second WT. Therefore, for the next two loops, U_∞ becomes $u_{in_{1|2}}$ (the perceived wind of the last two turbines) and this time our implementation must go through the superposition model block:

- **Superposition model**

  Input: Isolated WT wake
  Output: Wake velocity deficit for the two last wind turbines
  The Superposition model is only useful for the last two wind turbines. Indeed, this model is a wake superposition model. It allows to consider the impact of the previous wind turbine(s) on the turbine on which the wake deficit is developped.

Now that the methodology to apply is fixed, one can implement and calibrate the whole model.

Chapter 3

Calibration of the wake model parameters

This chapter study the parameters of the model, the calibration of it for a wind turbine and finally examine different relations to obtain an effective model without having to calibrate it. Then, this calibration is extended to the whole farm thanks to a superposition model. After that, the BEM is introduced in the model and by varying the freestream velocity, the final behaviour of the farm is analysed. Prior to that, for coherence and comprehension, a benchmark used for the rest of the work and a tool that will be useful for the comparison with BigFlow are generated.

3.1 Benchmark and tools

Benchmark

In order to comprehend the axes and placement of the turbines in the future figures, it is interesting to set a marker and locations for the turbines and to number them.

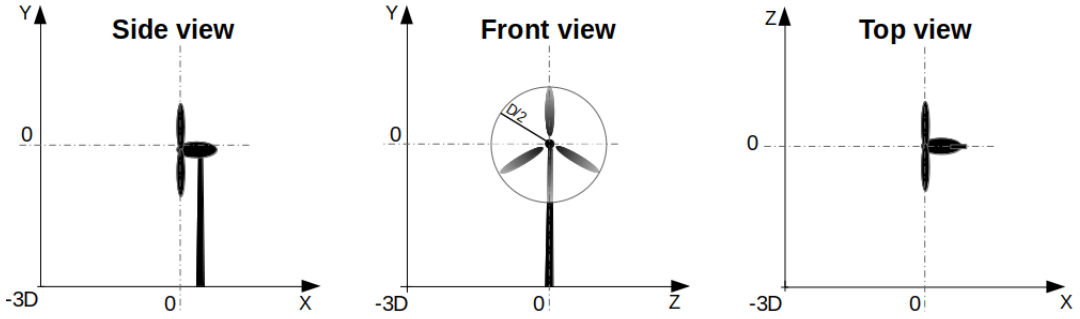

Figure 3.1: Representations of the position of a wind turbine according to the different views.

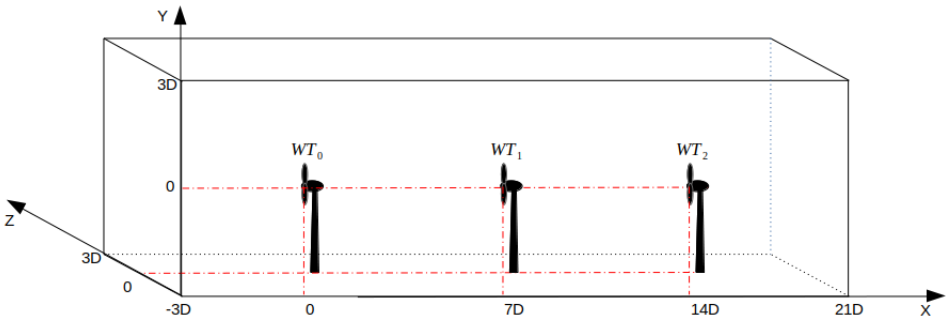

Figure 3.2: Multiple wind turbines positioning.

Tool : Mean Disk Velocity - MDV
To comprehend better the behaviour of the different parameters of the model, and to be able to compare the model to various BigFlow simulations, it is primordial to compare graphs following a certain methodology. Thus, a relevant tool is define: the Mean Disk Velocity (MDV). The MDV of a velocity field (only x-component for the velocity : $\mathbf{u} = (u,0,0)$) is the spatial average on a disk of diameter 1D which propagates in the streamwise direction. Thus, the domain of interest corresponds to a tube whose circular face of diameter 1D is centred in $(y,z) = (0,0)$ and whose tube length corresponds to the entire streamwise direction. This domain is represented in Fig. 3.4,3.3.

It is interesting to make an average on a 1D disk since it corresponds to the diameter of the rotor of the wind turbine. Thus, the model is calibrated to have the right mean wind speed in inflow of each wind turbine. This is important for two reasons: the first is that the wakes of a turbine depend on the inflow they perceive. A bad calibration of the inflow wind of a turbine will propagate the error to the other turbines, and the behaviour of the farm will not be consistent. The second is for the use of the farm's model for power calculation. Since this power is related to the wind speed at the input of the turbines, it is important that the inflow of each turbine is accurate.

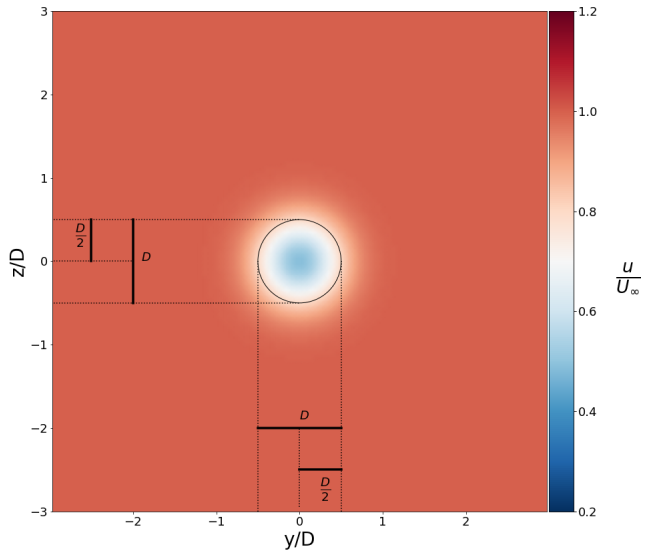

Figure 3.3: Compute the mean disk velocity averaging, slice $[\vec{y},\vec{z}]$.

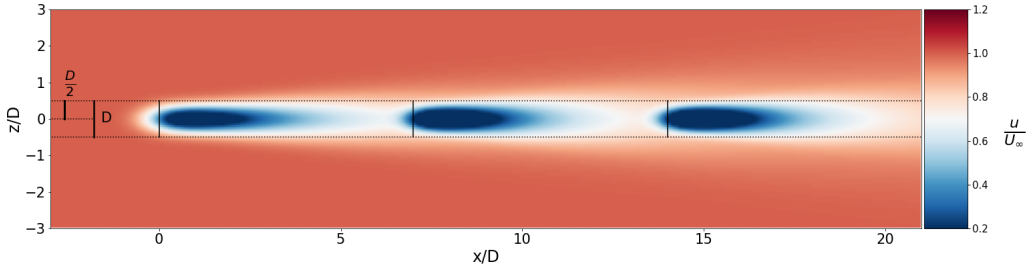

Figure 3.4: Compute the mean disk velocity averaging, slice $[\vec{x},\vec{z}]$.

For example, a kind of graph that can be obtained with this tool is shown in Fig. 3.5. In the following section, when the MDV is used, it will be specified in the caption by the initials MDV: (Mean Disk Velocity), followed by the classic legend. Now, our work has a relevant means of comparison and analysis. Since all these analyses are based on time-averaged simulations, the use of $\bar{u}$ will appear for the spatial MDV mean.

3.2 Impact of the model parameters

To understand how the Shapiro model works, it is interesting to see how the model outputs change with its parameters. Parameters that have an impact on the wake are the thrust coefficient C_T and the expansion coefficient k^*.

The first change is the thrust coefficient of the model. In Fig. 3.5, increasing the C_T create a "bigger drop". This means that a bigger C_T produce a bigger near wake deficit. Indeed, increasing the C_T means increasing the thrust directly, by conserving inflow conditions. By definition of this aerodynamic force, it acts against the flow. Thus, increasing this force slows down the wind flow, creating a more important deficit.

The thrust coefficient can be changed using two operating points. Indeed, this one depends on the Tip Speed Ratio (TSR or λ) and the pitch angle (β) : C_T~(λ, β).

$$\lambda = \frac{\omega \cdot R}{u_{in}} \quad [-] \tag{3.1}$$

Where :

- ω [rad/s] : rotational speed of the rotor.
- u_{in} [m/s] : perceived inflow speed of the turbine (equal to $U_\infty = 9$ [m/s] in our case).
- R = D/2 = 63 [m], radius, length of the blade.

In Fig. 3.5 the TSR of the Shapiro model (λ) is modified to a constant $k^* = 0.08$. For this three different TSR [5.7, 7.55, 8.86], the C_T are respectively equal to [0.647, 0.852, 0.953]. These C_T are computed from BigFlow simulations.

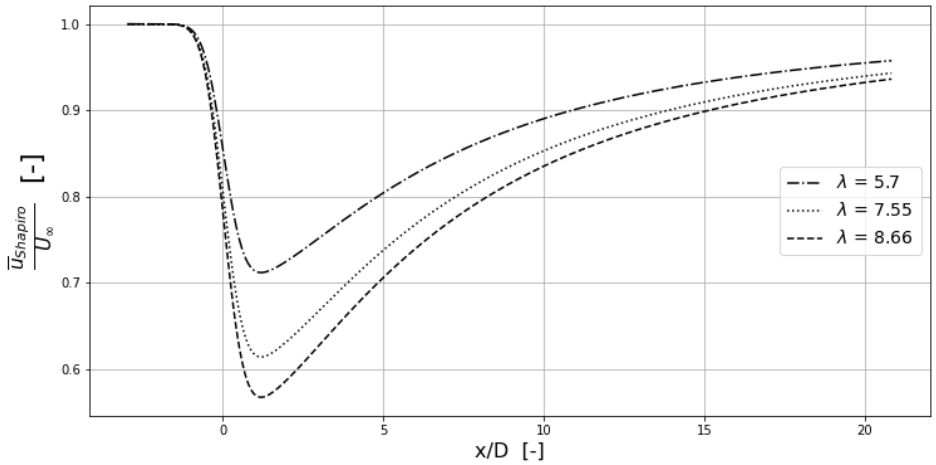

Figure 3.5: MDV : Impact of λ on wake behaviour at $k^* = 0.08$. Shapiro model - $U_\infty = 9\,[m/s]$

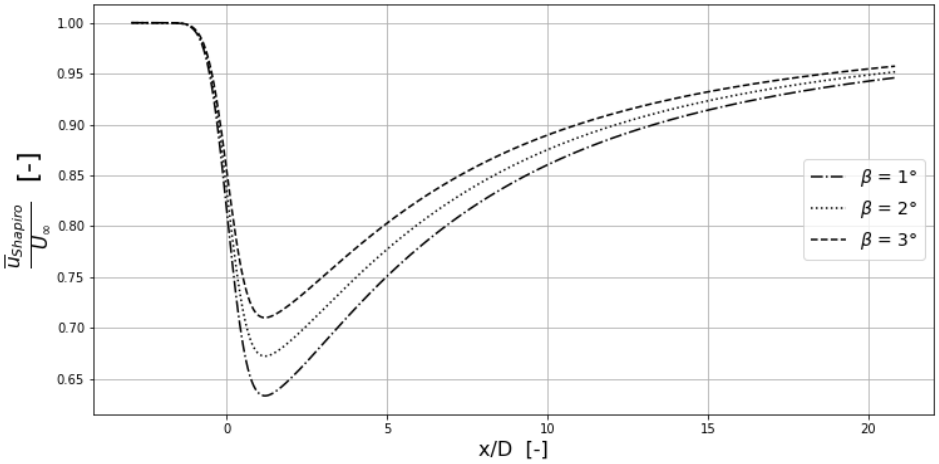

Figure 3.6: MDV : Impact of β on wake behaviour at $k^* = 0.08$. Shapiro model - $U_\infty = 9\,[m/s]$.

In Fig. 3.6 the same MDV analysis was performed. But this time, instead of modifying the C_T with λ, it is modified with β. The three chosen values are $\beta = [1°, 2°, 3°]$ corresponding respectively to $C_T = [0.791, 0.726, 0.659]$. Increasing the pitch angle therefore implies a decrease in C_T which results in a smaller deficit in the near wake. The reason is the higher the pitch, the more the blades allow the wind to pass through the WT, thus creating a lower deficit just after it.

The wake's depictions in Fig. 3.7 confirm the observations made in Fig. 3.5, 3.6. Indeed, the higher the C_T (i.e. the higher λ or the lower β), the higher deficit in the near wake region.

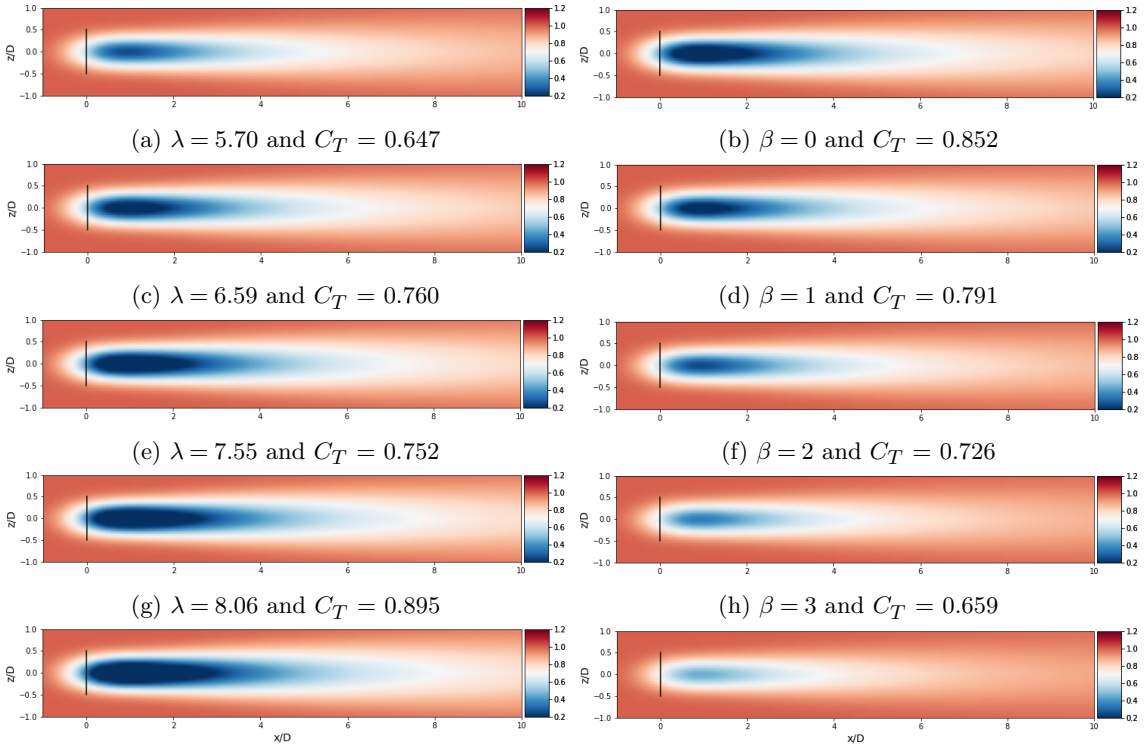

(a) $\lambda = 5.70$ and $C_T = 0.647$

(b) $\beta = 0$ and $C_T = 0.852$

(c) $\lambda = 6.59$ and $C_T = 0.760$

(d) $\beta = 1$ and $C_T = 0.791$

(e) $\lambda = 7.55$ and $C_T = 0.752$

(f) $\beta = 2$ and $C_T = 0.726$

(g) $\lambda = 8.06$ and $C_T = 0.895$

(h) $\beta = 3$ and $C_T = 0.659$

(i) $\lambda = 8.86$ and $C_T = 0.953$

(j) $\beta = 4$ and $C_T = 0.590$

Figure 3.7: Representation of ${}^{U_{wake}}/_{U_\infty}$ for $k^* = 0.08$. Shapiro model - $U_\infty = 9\,[m/s]$. Slice at hub height (y = 3D).

The second parameter to investigate in the model is the expansion coefficient k^*. In Fig. 3.8, the C_T is held constant and the expansion coefficient assigned to 5 different values. This graph shows

us that the expansion coefficient has an impact on the wake recovery rate. A higher expansion coefficient causes a faster wake recovery. Indeed, for a k^* of 0.02 the model reach $0.7 \times U_\infty$ for a downstream distance $\approx$ 18D while it is already reached at $\approx$ 4D for a k^* of 0.1. In Fig. 3.9 the same observation is made when analysing the wakes at y = hub height. Indeed, the smaller the k^*, the more difficult it is for the wake to evolve towards the initial value of $U_\infty = 9$ [m/s]. So for a value of $k^* = 0.02$ in Fig. 3.9a, the deficit is more spread out in the streamwise direction than for $k^* = 0.1$ in Fig. 3.9e.

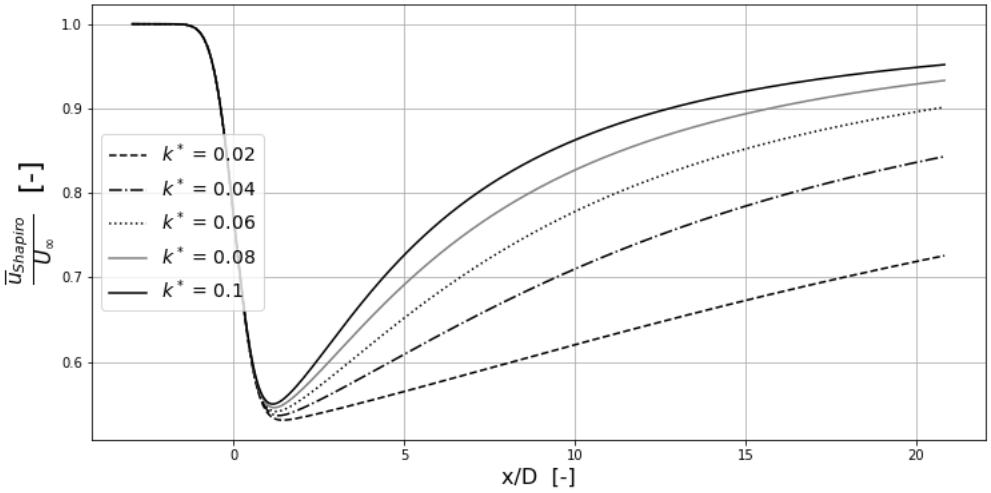

Figure 3.8: MDV: Impact of k^* on wake behaviour at $C_T = 0.8$. Shapiro model - $U_\infty = 9$ [m/s].

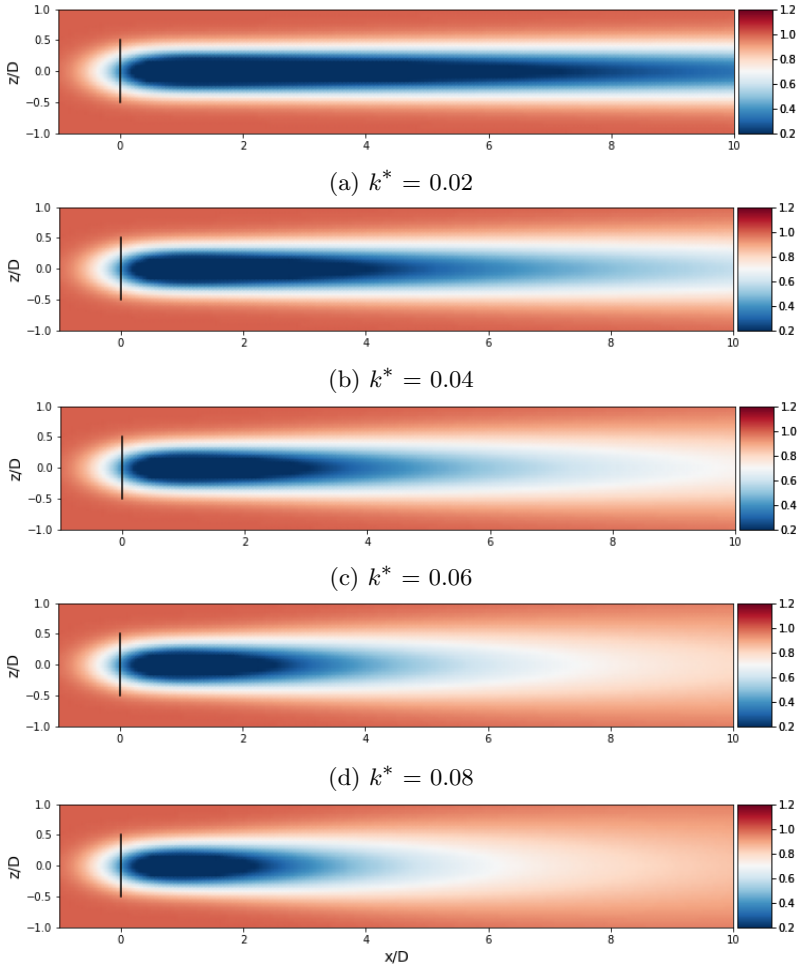

(a) $k^* = 0.02$

(b) $k^* = 0.04$

(c) $k^* = 0.06$

(d) $k^* = 0.08$

(e) $k^* = 0.1$

Figure 3.9: Expansion coefficient impact on Shapiro model with $C_T = 0.8$ at y = hub height. Shapiro model - $U_\infty = 9$ [m/s].

Now that the impact of C_T and k^* on the wake model have been exterminated, these parameters can be tuned in order to fit the MDV curves of the model on the BigFlow ones.

3.3 Investigation of the expansion coefficient for isolated wind turbines

The purpose of this section is to see if it is possible to calibrate the expansion factor and to have a shape of the wake corresponding to the one of BigFlow at a distance of 7D from the turbine.

3.3.1 Expansion coefficient calibration

As discussed in Section 3.2, there are two parameters that affect the wake behaviour: C_T and k^*. The experiment that is performed is to compare the BigFlow simulation and the wake model, in particular their MDV. As the parameter C_T will be given later by the BEM, the expansion coefficient is adjusted with C_T fixed (for the studied case) and given by the BigFlow simulation. The 2 MDV (model and BigFlow) can be compared at same operating points. Then, one can check whether the near wake deficit due to C_T is comparable to the one of BigFlow and analyse whether there is an expansion coefficient k^* for which our error at $x = 7D$ is relatively small. The error is simply defined as the difference between the MDV (for the whole streamwise direction) of BigFlow

and the model, normalized by the freestream velocity : $E = \frac{\bar{u}_{BF} - \bar{u}_{model}}{U_\infty}$.
Therefore, the closer the two MDV are, the smaller the error.

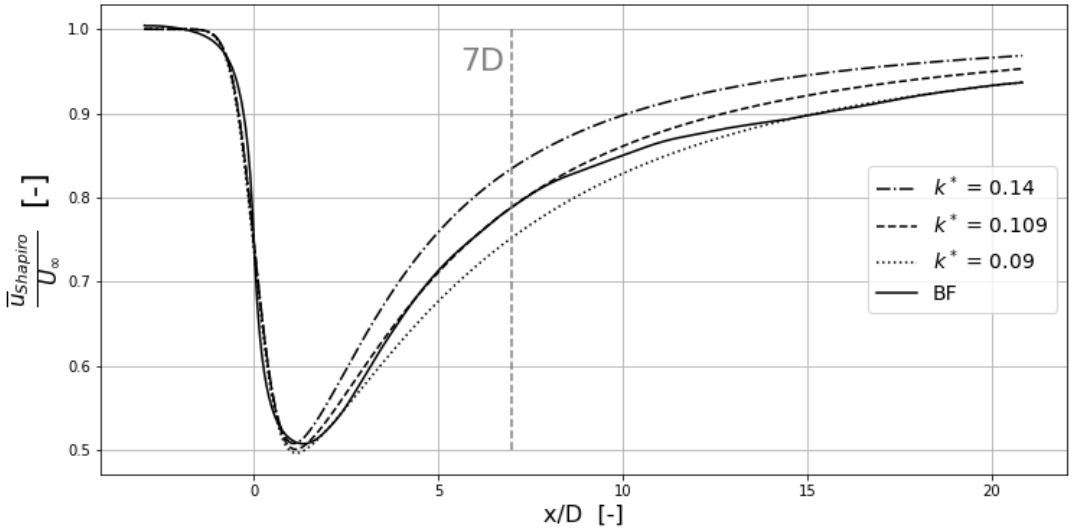

Figure 3.10: MDV: BigFlow and Shapiro model for three values of k^* at $\lambda = 7.55$. $U_\infty = 9$ [m/s].

Fig. 3.10 shows that several k^* may be appropriate for the two models to match. It all depends on where we want the curves to be the closest. The dotted curve would therefore give good values for relatively large distances (x > 15D). The interesting curve is the dotted. Indeed, this one has a similar behaviour (same spatial average velocity) to the one of BigFlow at a distance downstream of the WT equal to 7D. Having a low error at x = 7D is important for two reasons (as explained before). The first is that, since the next turbine is at this position, it is important to have the right wind speed for power computation. The second reason is that the wake model depends on the inflow. Thus, a bad calibration would lead to a wrong wake computation for all downstream turbines.

As seen in Tab.3.1, there is a non-negligible variation of k^* as a function of λ (and thus of C_T). The k^* fitting is done by computing the error (using MDV) for forward distance ranging from $x = 5D$ to $x = 7D$. Several types of calibration could have been performed. Indeed, our model could have calibrated with k^* on a single downstream position ($x = 7D$). This calibration is, however, less general and would not allow a change in distance between turbines if it were desired. The method used to calibrate the model allows us to get a wake recovery relatively similar to the desired one. In Fig. 3.11, the choice of calibration is illustrated. As can be seen, the error is minimal for the studied field (i.e. $x = 5D$ to $x = 7D$).

	k^*	4D			6D		
		$\bar{u}_{model}$ [m/s]	$\bar{u}_{BF}$ [m/s]	Error [%]	$\bar{u}_{model}$[m/s]	$\bar{u}_{BF}$ [m/s]	Error [%]
TSR 5.7	0.0645	6.54	6.47	1.08	6.97	7.06	1.27
TSR 7.55	0.109	5.95	5.93	0.33	6.797	6.82	0.33
TSR 8.86	0.145	6.026	5.82	3.53	6.77	6.76	0.207

	k^*	7D		
		$\bar{u}_{model}$ [m/s]	$\bar{u}_{BF}$ [m/s]	Error [%]
TSR 5.7	0.0645	7.16	7.29	1.82
TSR 7.55	0.109	7.110	7.12	0.196
TSR 8.86	0.145	7.06	7.07	0.14

Table 3.1: Analysis of parameters such as k^* (calibrated), the spatial average speed of our implementation and BF (using local MDV) noted $\bar{u}_{model}$ and $\bar{u}_{BF}$, and the obtained error calculated as: $(100\% \cdot {}^{(\bar{u}_{Shapiro} - \bar{u}_{BF})}/_{\bar{u}_{BF}})$ at three distances [4D, 6D, 7D]. $U_\infty = 9$ [m/s].

The Tab. 3.1 shows the velocities obtained for several distances downstream of the turbine after the calibration of the k^* with the method explained before. The velocities of BigFlow and of the Shapiro model are very close to each other, especially at $x = 7D$, the distance of interest. The maximum fluctuation appears between velocities of 1.82 [%]. This fluctuation is quite small and will therefore have a negligible impact on the future downstream wind turbines.

Since the output power supplied by the wind is proportional to the cube of its speed, the error in power can be calculated as:

$$P \propto \bar{u}^3 \qquad (3.2) \qquad\qquad E_P \propto (\bar{u}_{Sh}^3 - \bar{u}_{Bf}^3)/(\bar{u}_{BF}^3) \qquad (3.3)$$

With E_P the power error. When calculating this error for the maximum speed variation ($\lambda = 5.7$), this gives: $E_P = 5.2$ [%]. This value is therefore the maximum error in power provided by the wind at 7D for different values of λ. However, this error is still appropriate. Furthermore, the ultimate goal of this work is to reach maximum output power of the farm. The operating point to reach this goal, at $U_\infty = 9$ [m/s], is at higher TSR than 5.7 at first sight.

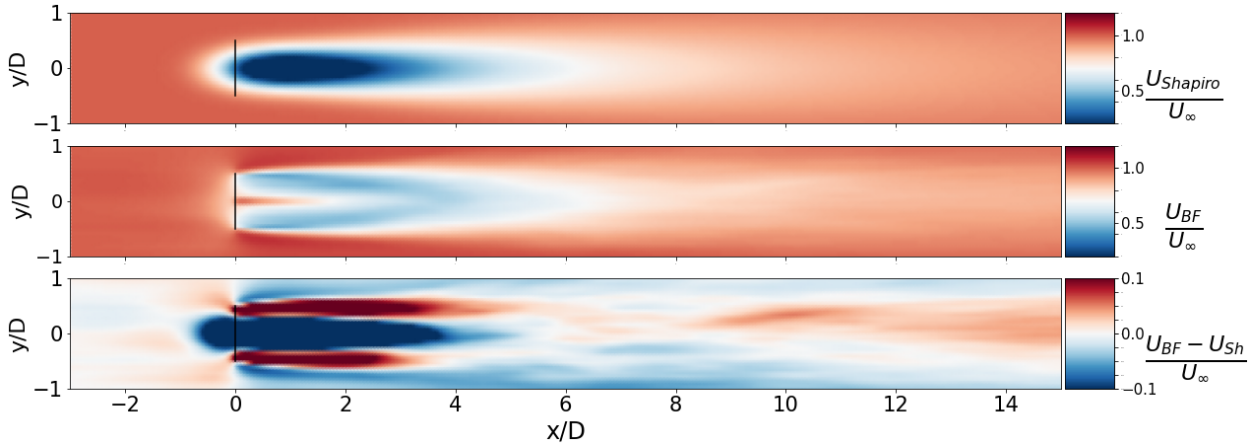

Figure 3.11: Representation of the Shapiro wake model, a BigFlow simulation, and the difference between these two wakes at hub height. $\lambda = 7.55$, TI = 6% and $k^* = 0.109$ at 9 [m/s].

Now that the k^* has been calibrated, one can check with the wakes that our adjustment works. In Fig. 3.11, the last colormesh represents the difference between BigFlow and Shapiro model ($\lambda = 7.55$ and so $k^* = 0.109$). This graph allows seeing that from five diameters, the two wakes have similar behaviour. This graph also shows that the shape of the wake model in the near wake does not correspond to reality. It is therefore interesting to see how the wake profile evolves as a function of the distance. The following section will address this.

3.3.2 Wake profile

The wake profile is not very important when using a Uniform Inflow BEM (UI BEM). In this case, only the amplitude of average speed of the inflow is significant since it is directly the input to the UI BEM as a single value. However, our model will use a Non-Uniform Inflow velocity (NUI BEM) to compute more precisely the loads according to the NUI (these UI and NUI BEM are explained in the section 3.6). When using a NUI BEM, it is important to have a wind distribution consistent with that of BigFlow. Therefore, the wake profile of the model and BigFlow will be compared.

Within this section, we base the rest of our analysis of the shape on a $\lambda = 7.55$ [-], which is the classical value when working at a wind speed of 9 [m/s]. The corresponding k^* is equal to 0.109 (Tab. 3.1).

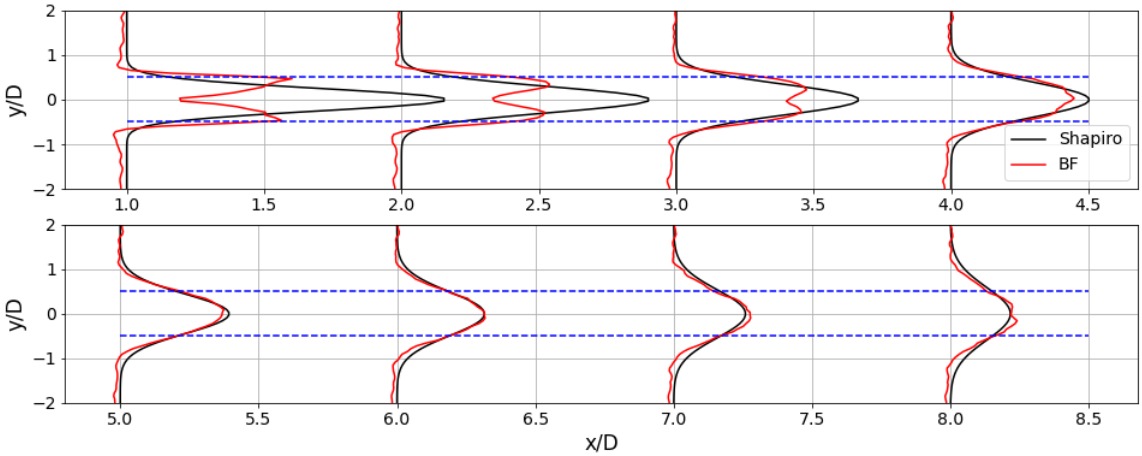

Figure 3.12: Shape of the velocity deficit development at y = hub height. $\lambda = 7.55$ and $k^* = 0.109$. Shapiro model - $U_\infty = 9$ [m/s].

In near wake, the development of the velocity deficit is not identical for both models (Fig. 3.12). Indeed, the Shapiro model is based on a Gaussian shape which evolves and flattens. The BigFlow near wake simulations has a hub jet that our model does not represent. The hub jet is noticeable only for a very short distance behind the rotor. The appearance of this hub jet comes from the modelling of the Actuator Disk : the AD is defined from $r = R_{hub}$ to $r = R_{Tip}$. So, the AD is hollow at its centre ($r = 0$ to $r = R_{hub}$). The deficit is therefore lower at the centre of the wake.

After a few diameters behind the WT, BigFlow's simulation approaches the Gaussian form developed in the Shapiro model. At $x = 7D$, the velocity distribution is very close to the BigFlow one. Since the graph in Fig. 3.12 is not axisymmetric, it is not possible to conclude about the accuracy of the model shape, but it gives a good idea of the spread of the deficit. One can see what happens when an azimuthal average is done.

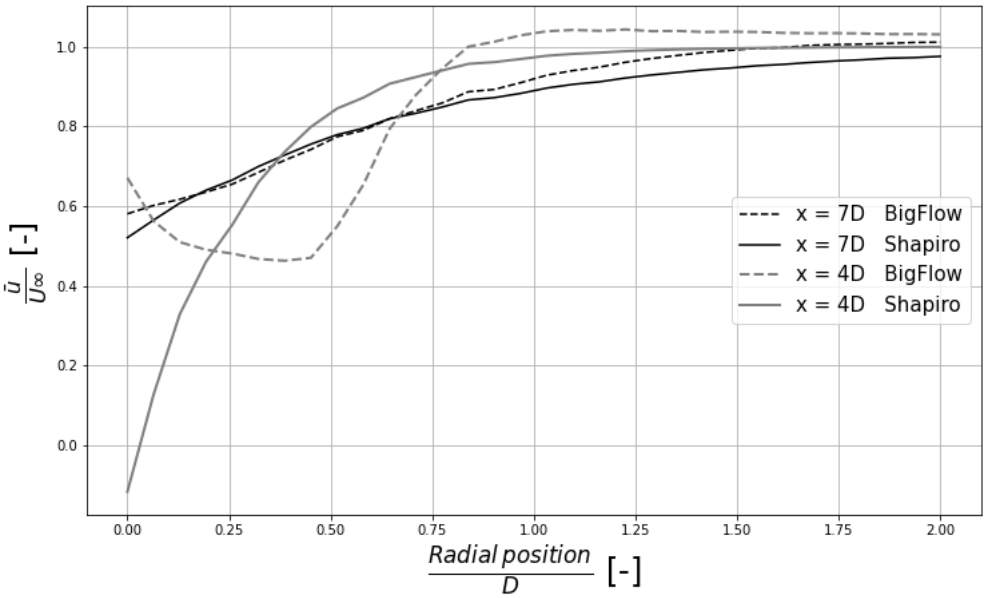

Figure 3.13: Azimuthal mean of the streamwise velocity according to radial position. Shapiro model - 9 [m/s].

Fig. 3.13 corresponds to the azimuthal average of the wind speed according to the radial position, for two positions in the streamwise direction ($x = 4D$ and $x = 7D$). This consists in averaging this velocity on a circle centred on the rotor, with an evolving radius (from 0 to 2D in our case). This plot shows that, at more than 7D downstream of the WT, the wake profile of Shapiro is relatively close to the BigFlow one in terms of behaviour and amplitude.

In Fig. 3.13, we still observe the presence of the hub jet at $x = 4D$ whereas it does not appear in Fig. 3.12. Thus, the behaviour of the Shapiro model does not correspond to the one expected. Indeed, the Shapiro model only assume the wake profile to be Gaussian (without hub jet). The presence of this hub jet can be observed because the minimum of the velocity is at $r/R = 0.4$ and not at the centre, as it is the case for the Shapiro (Gaussian) model. To see the evolution of the error on velocity profiles, the azimuthal averaging between BigFlow and Shapiro profiles are computed for diameters ranging from $x = 4D$ to $x = 7D$. (Fig. 3.14).

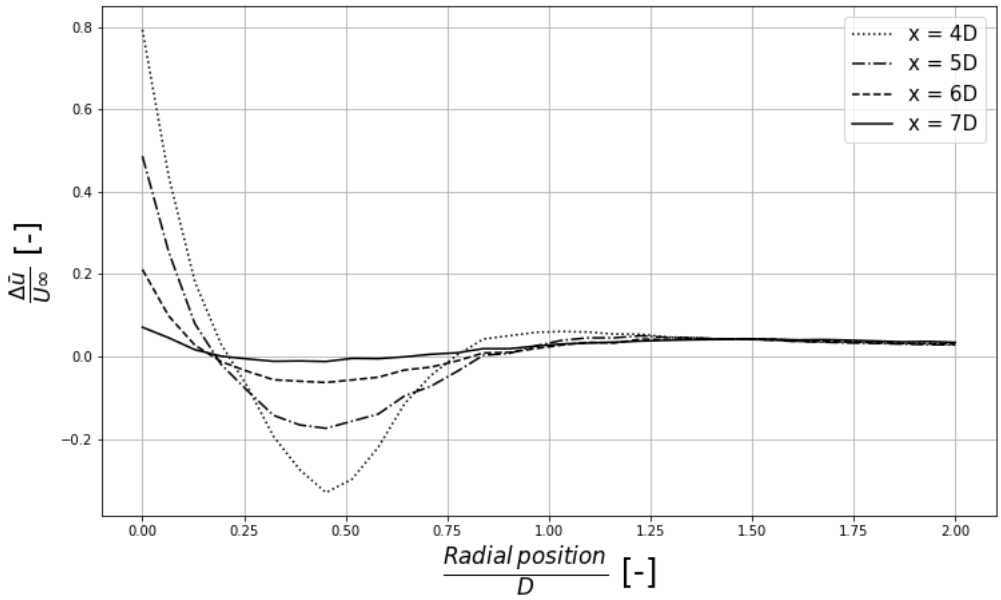

Figure 3.14: Azimuthal mean error $^{\Delta\bar{u}}/_{U_\infty} = {}^{(\bar{u}_{BF} - \bar{u}_{Sh})}/_{u_\infty}$ of the streamwise velocity according to the radial position. Shapiro model - 9 [m/s].

As seen in Fig. 3.12, the further along the streamwise direction of the BigFlow simulation, the more the jet hub attenuates and the more the time averaged deficit looks like a Gaussian. The error $\Delta\bar{u} = \bar{u}_{BF} - \bar{u}_{Sh}$ thus weakens with the increase of the streamwise distance. The index *Sh* stands for *Shapiro*.

As expected, Fig. 3.14 shows that from $x = 4D$ to $x = 7D$ the difference between the two wakes decreases and is close to zero when it reaches $x = 7D$. This enable to conclude that at 7D the distributions of the deficits in the wakes are relatively similar and that,therefore, the use of a NUI BEM is possible.

It is important to note that the adjustment of the k^* also varies the azimuthal error. As seen in Fig. 3.10, the coefficient $k^* = 0.109$ gives good results for the amplitude of the mean streamwise velocity in the studied field.

Now that our Shapiro model is calibrated (with k^*) and that the fidelity of the wake profile is confirmed, one can find relationships so that the value of the k^* can be acquired by calculation, for various cases. This is the purpose of the next section.

3.4 Establishment of the wake model for isolated wind turbines

The aim of this section is to find a relationship that can link the expansion coefficient to some parameters. This permit to obtain a k^* without having to calibrate it for each case. To do this, one can analyse in more details useful relationships.

3.4.1 Study at various operating points and conditions

Relation $C_T - k^*$

The relationship linking k^* with C_T is a very important relationship. In paper [22], they use an equation linking the induction factor to the k^* to calibrate their model. Since the induction factor evolves in the same way as the C_T, this justifies the need to use the C_T (or the induction factor) to calibrate the k^*.

Indeed, as seen in the section 3.2, when varying the C_T for the same k^* (Fig. 3.5),the curves do not coincide at the same point 7D downstream the WT, whereas it is the case (more or less) for the BigFlow simulation (Fig. 3.15).

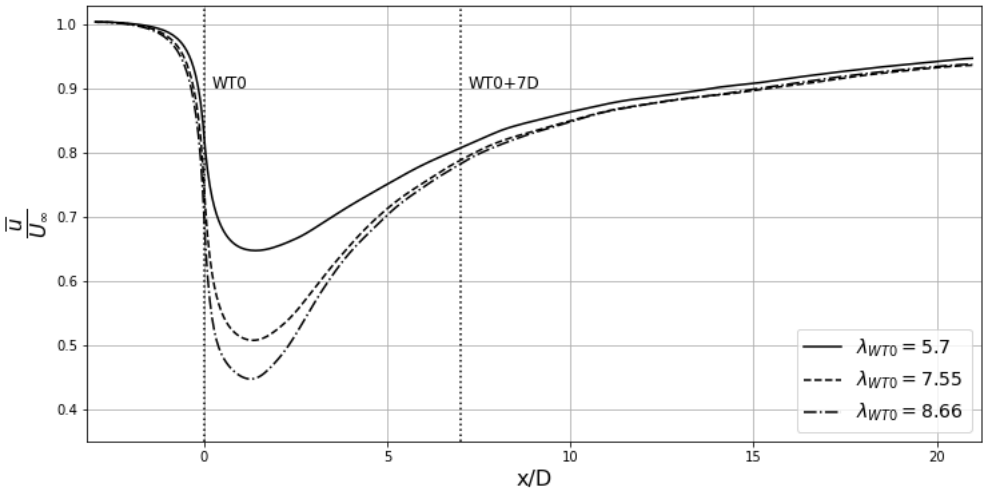

Figure 3.15: MDV: Variation of the C_T factor via the parameter λ and representation of its impact on the wake for the first wind turbine. Shapiro model - 9 [m/s].

Fig. 3.5 & 3.15 reveal that the behaviours of the BigFlow and Shapiro wake are not maching. Indeed, when the C_T of our model vary, the different curves do not join together (Fig. 3.5) as it is the case, for the same experiment, in the BigFlow simulations (Fig. 3.15). This could perhaps be explained by the arbitrary choice of the coefficient k^* of the Shapiro model which was equal to 0.08. In fact, it is not the case. In order to show that the particular $k^* = 0.08$ is not responsible for this problem, the experiment for different k^* is reproduced, and again the curves do not meet either. These results are available in Appendix A.1. Seeing that the curves do not join, our model must include a $C_T - k^*$ relation to counteract this problem.

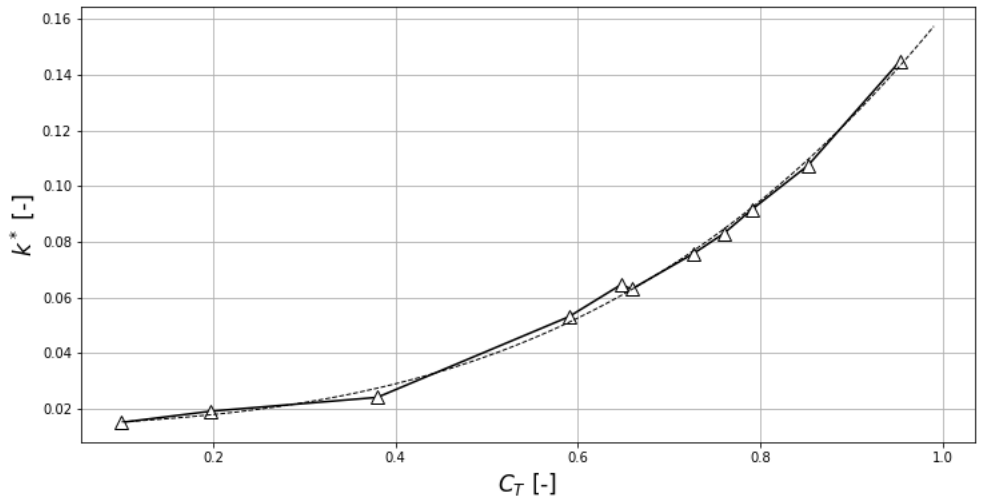

Figure 3.16: Relation between the thrust coefficient C_T and the expansion coefficient k^*, at fixed operating condition : TI 6%, $U_\infty = 9$ [m/s].

In order to obtain the relation related to the Fig. 3.16, the calibration of several k^* as a function of thrust coefficient has been performed at operating conditions : $U_\infty = 9$ [m/s] and $TI = 6$[%].

This calibration is made as explained in the section 3.3. Indeed, k^* is calibrated by comparing the Shapiro model and the BigFlow simulations for the same C_T (compute using BigFlow). Doing that make possible to only calibrate k^*, without taking into account the possible variation in the computation of C_T (if it was calculated by our BEM). It allows to process one variable at a time. These C_T are obtained by changing either the λ or the β as input of the BigFlow simulation.

Plotting the data on a graph (Fig. 3.16), display that the k^* is necessarily linked to the C_T. Thus, the curve linking the expansion coefficient to the thrust coefficient can be interpolated. It is therefore fairly easy to derive a relationship :

$$k^* = k^*(C_T)|_{TI_{6\%}} \tag{3.4}$$

A 3^{rd} order interpolation gives us :

$$k^* = 0.123 \cdot C_T^3 + 0.009 \cdot C_T^2 + 0.0149 \cdot C_T + 0.013 \tag{3.5}$$

Thanks to this relation, the expansion coefficient to be applied for a certain thrust coefficient is known. However, this relation can only be used for a TI 6 % (as the freestream velocity U_∞, we call it TI_∞ since it is the turbulence intensity at the entrance of the domain). Wind turbines create a lot of shear stress and vortices downstream, which leads to a lot of turbulence. It is therefore interesting to see what happens to k^* with other TI in order to model the wake conditions (for the second and third WT) at constant C_T.

Relation $TI_\infty - k^*$

As explained in the section 2.3, the expansion coefficient is assumed to increase with the TI. Indeed, the wakes will recover faster with an increase of the ambient turbulence intensity. Because higher incoming turbulence enhances mixing processes, which results in a faster wake recovery. This theory is verified in the graph of Fig. 3.17 for a constant C_T. This C_T corresponds to the classical value for U_∞= 9 [m/s] and $\lambda = 7.55$, $\beta = 0$.

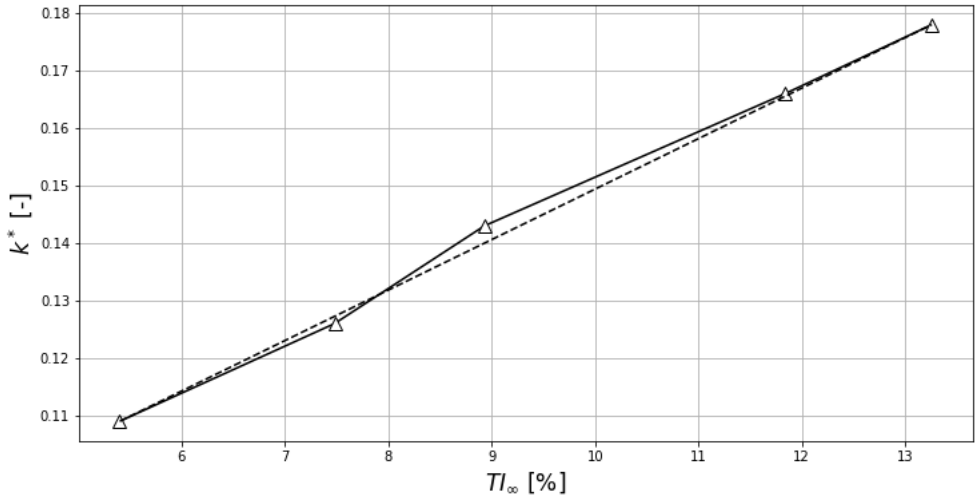

Figure 3.17: Relation between TI_∞ and k^* with $C_T = 0.852$. $U_\infty = 9$ [m/s].

The factor k^* evolves following a linear relation according to the TI_∞ whose equation is:

$$k^* = 0.00883 \cdot TI_\infty + 0.0615 \tag{3.6}$$

In order to be able to use these two relations (Eq. 3.5 and Eq. 3.6) for the computation of k^*, it is necessary to verify that these two equations are independent of each other, and thus that the value of $C_T \perp\!\!\!\perp TI_\infty$. We will see that in the next section.

Relation $TI_\infty - C_T$

As a way to compute k^*, one can try to combine the two equations found in previous sections:

$$k^* = k^*(C_T)|_{TI_{6\%}} \tag{3.7}$$

$$k^* = k^*(TI)|_{C_T=0.852} \tag{3.8}$$

To combine these two equations, they must not be correlated (i.e. TI_∞ does not have an impact on the C_T value). In case of correlated equations, the TI/C_T dependence would be taken twice into account. So, we must verify that $C_T \perp\!\!\!\perp TI_\infty$

.

In the graph of Fig. 3.18 the C_T varies very little with the value of the TI_∞. For the extreme values of TI_∞ in the graph, the C_T fluctuates between 0.85 and 0.87. Therefore the hypothesis: $C_T \perp\!\!\!\perp TI_\infty$ can be assumed. Eq. 3.5 and Eq. 3.6 are therefore combined in the next section.

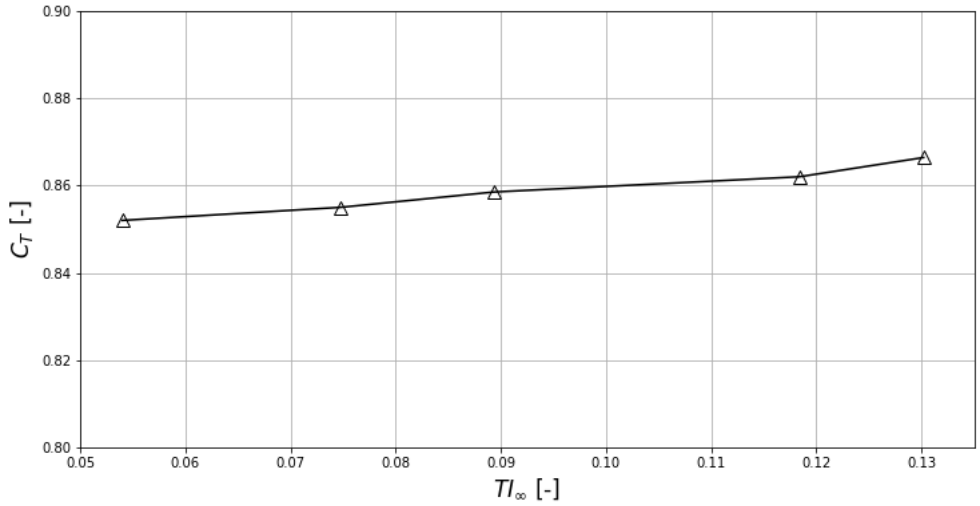

Figure 3.18: Relation between TI_∞ and C_T - BigFlow simulations data.

3.4.2 Expansion coefficient: final expression

To assemble the two equations, we start with the relation C_T - k^* (Eq. 3.16) and the goal is to find a multiplicative factor (which depends on the TI_∞) that will multiply the k^* obtained with the $C_T - k^*$ relationship. This leads to the following equation:

$$k^* = (0.123 \cdot C_T^3 + 0.009 \cdot C_T^2 + 0.0149 \cdot C_T + 0.013) * TI_{factor} \tag{3.9}$$

Where:

$$TI_{factor} = \frac{k^*(TI_\infty)}{k^*(TI_{ref})} = \frac{a \cdot TI_\infty + b}{a \cdot TI_{ref} + b} \tag{3.10}$$

With :

- a and b corresponding to the coefficients of the linear relation (Eq. 3.6 - a = 0.00883 and b = 0.0615).
- TI_∞ corresponding to the "freestream" TI of the farm (operating condition)
- TI_{ref} corresponding to the reference TI = 6 %, (TI used to evaluate the relation $C_T - k^*$)

The final equation (Eq. 3.9)permit to have an approximate k^* as a function of the variables C_T and TI_∞. To analyse if our equation gives us an appropriate k^* value by varying the TI_∞, C_T, and both simultaneously, one can move to the next section.

3.4.3 Results analysis

To analyse the results, we will first check that each of the relationships is working correctly independently of each other. By doing so, we could understand where potential errors might come from.

An analyse of the relation $C_T - k^*$ for various C_T at TI = 6% is done in Fig. 3.20. First of all, the velocity drop in the near wake region does not correspond exactly to the BigFlow one. This disparity is due to the fact that the $TI_{near\,wake}$ depends on the C_T. Indeed, we use the term $TI_{near\,wake}$ since the thrust induces turbulence just downstream the turbine. The larger the C_T is, the larger the $TI_{near\,wake}$ will be. It is this $TI_{near\,wake}$ just after the wind turbine that impacts the near wake velocity drop. The Shapiro model does not take this $TI_{near\,wake}$ into account, it creates a difference between the two models. As far as the amplitude of the streamwise velocity at 7D is concerned, this one is relatively well gauged, confirming that our C_T - k^* relation is a good approximation.

Now, the TI_{factor} for 3 different TI (6%, 10%, 15%) will be evaluated to see if the outcome is the desired one (Fig. 3.21). The figure corresponding to TI 6% match to the one in Fig. 3.20b. On these images, regarding the velocity drop in the near wake, the same observation as before can be made. Indeed, the $TI_{near\,wake}$ also depends on the input TI (TI_∞) leading to the same conclusion as the previous ones. It can also be seen that, as before, the velocity amplitude at 7D downstream of the wind turbine is relatively equivalent to that of BigFlow.

The problem resulting from the drop in near wake for the same values of C_T, will create, for simulations with high C_T and high TI_∞, velocity behaviours in near wake which do not match very well to reality. We can see what happened for $C_T = 0.96$ and TI = 10% (Fig. 3.19). In this figure, the location of the calibration performed (between 5D and 7D) can easily be detected, this one corresponds to the intersection of the two curves. Since the velocity drop in the near wake does not match that of BigFlow, the wake behaviour is less realistic, even if the k^* is close to the desired one. But knowing that the near-wake region is not important for power, we can consider that Fig. 3.19 gives convincing results.

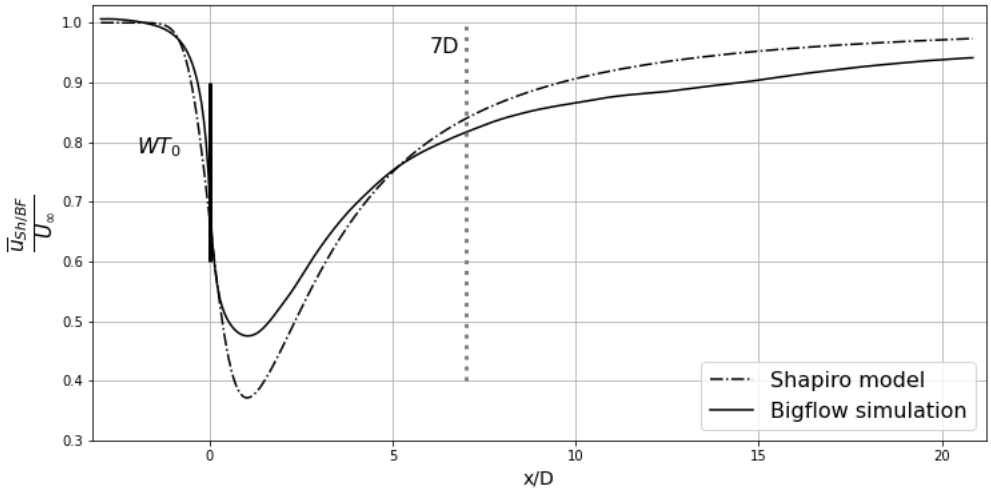

Figure 3.19: MDV: Shapiro and BigFlow models at TI 10 % and $TSR = 8.86$ corresponding to $C_T = 0.953$ using our relation to calculate k^*. $U_\infty = 9$ [m/s].

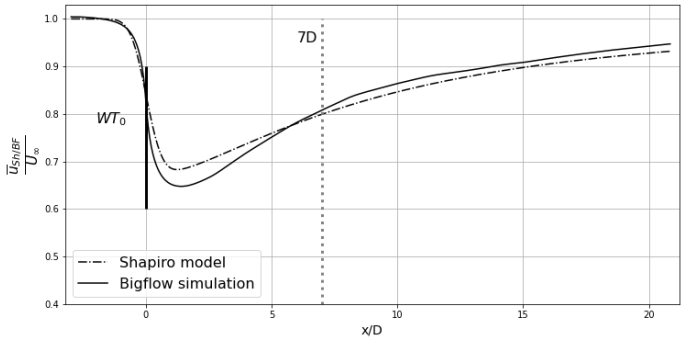

(a) $C_T = 0.647$

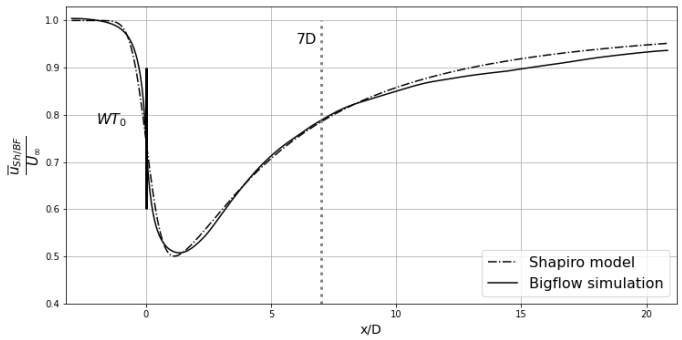

(b) $C_T = 0.852 \rightarrow$ TI = 6%

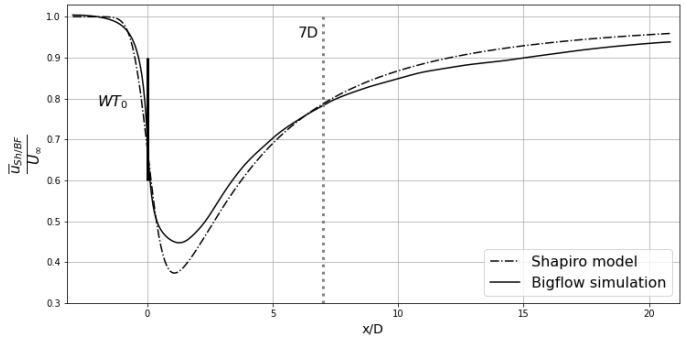

(c) $C_T = 0.953$

Figure 3.20: MDV: Evolution of Shapiro and BigFlow models at TI 6% for various C_T using our relation to calculate k^*. $U_\infty = 9$ [m/s].

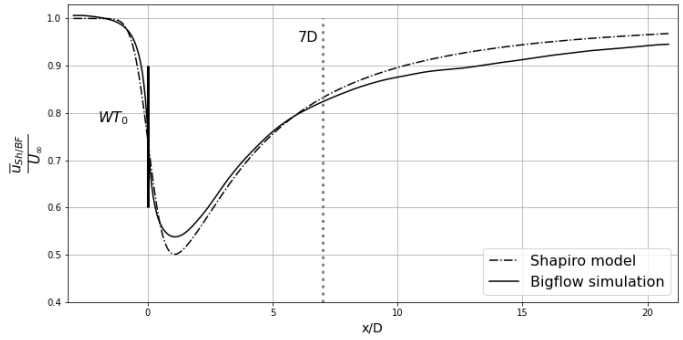

(a) TI = 10%

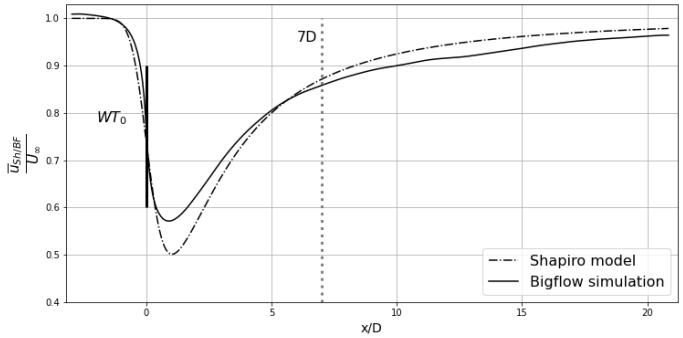

(b) $TI = 15\%$

Figure 3.21: MDV: Evolution of Shapiro and BigFlow models at $C_T = 0.852$ for various TI_∞ using our relation to calculate k^*. $U_\infty = 9$ [m/s].

Now that our final k^* relation is determined, one can compare it to the literature to see if it gives better results.

3.4.4 Comparison of the expansion coefficient with the literature

In the literature, the k^* factor is usually calculated as a function of the TI. In Haohua Zong and Fernando Porté-Agel [24], it is approximated as:

$$k^* = 0.38 \cdot (TI_\infty^2 + TI_+^2)^{1/2} + 0.004 \tag{3.11}$$

With:

$$TI_+ = 0.73a^{0.83} \cdot TI_\infty^{0.03} \cdot (x/D)^{-0.32} \tag{3.12}$$

This equation with the $\lambda_{WT0} = 7.55$ with a simulation of one turbine can be exploited:
In this case: $C_T = 0.852$, $TI_\infty = 0.566$ and x = 7D

With:

$$a = \frac{1}{2}(1 - \sqrt{1 - C_T}) \tag{3.13}$$

Giving:

$$a = 0.30 \qquad TI_+ = 0.1322 \qquad k^* = 0.0586$$

Entering the value of k^* in the Shapiro model provides :

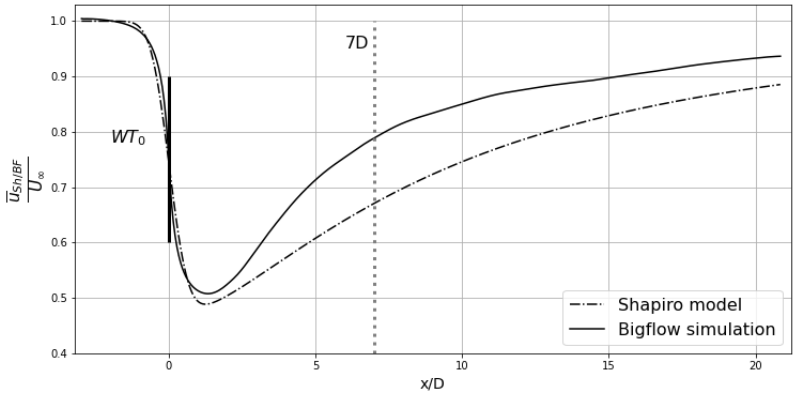

Figure 3.22: MDV : k^* proposed by H. Zong and F. Porté-Agel [24], using C_T from BigFlow. U_∞ = 9 [m/s].

In Fig. 3.22 the two curves do not match. The reason for this inconclusive result is that the equation to find the multiplicative factor is particular to a situation that does not correspond to ours. Indeed, the wind turbines used are not the same. Seeing that the results for the first wind turbine is already not conclusive, there is no point in pushing our analysis for the next two wind turbines.

The Shapiro model [23], uses experimental data to fit the k^*. They find that $k^* = 0.0834$. First, this relationship does not depend on any parameter. For our situation, it is not feasible for the expansion coefficient k^* to be constant (as shown in the fit of k^* Tab.3.1). However it is interesting to test this value to see what it gives at $\lambda = 7.55$.

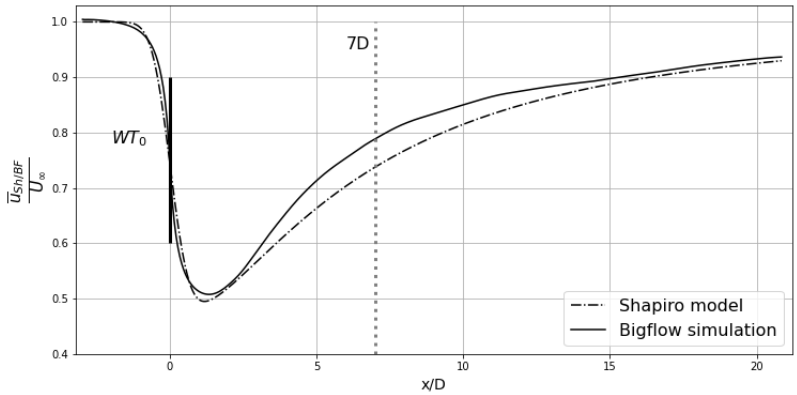

Figure 3.23: MDV : k^* proposed by the paper [23]: Carl R. Shapiro, Dennice F. Gayme and Charles Meneveau, using C_T from BigFlow. U_∞ = 9 [m/s].

This result is not conclusive either compared to the outcome achievement with our equation (As seen in Fig. 3.10 with $k^* = 0.109$).

The previous results show that it is interesting to make our own model to obtain results closer to those of BigFlow, and thus have an optimization that makes sense.

Now that our expansion factor gives us good results (better than the literature in our case), the goal is to find a way to extend the expansion factor for the last two WTs. To do this, the previous equations of k^* Eq. 3.9 can be reused. Thus, it is required to find a way to compute the TI = TI_{in} for these WTs in order to find the TI_{factor}. Indeed, the inflow TI of the last two turbines are not equal to the first of the farm: TI_∞.

3.4.5 Prediction of the turbulence intensity

As explained before, finding the TI at 7D downstream the WT (corresponding to the inflow TI (TI_{in}) of the next WT) is mandatory to reprocess the equation of k^*. It is relatively difficult to calculate the TI 7D downstream the WT. In the literature, it is usually approximated as:

$$TI(x) = \sqrt{TI_{in}^2 + TI_+(x)^2} \tag{3.14}$$

Where:

- TI_{in} is the inflow TI of the WT (equal to TI_∞ for the first one)
- TI_+ is an added TI depending on the operating parameters of the WT and the distance from it.

The added TI is relatively difficult to find. The literature presents different equations to approximate it. As presented in [13] (M. GE, Q. Zhang Li Li, Z Huang), the added TI can be approximated using two equations (named *Lit1* and *Lit2* respectively in Tab.3.4,3.5) as:

$$TI_+ = \frac{1}{1.5 + \frac{0.8}{\sqrt{C_T}}\frac{x}{D}} \tag{3.15}$$

$$TI_+ = 0.73(\frac{1-\sqrt{1-C_T}}{2})^{0.8325}(TI_\infty)^{0.0325}(x/D)^{-0.32} \tag{3.16}$$

With:

$$TI = \sqrt{TI_+^2 + TI_\infty^2} \tag{3.17}$$

Eq. 3.15 is calculated without taking into account the TI_∞ perceived by the wind turbine.

The results of the literature and the results obtained with BigFlow by averaging the TI on a one diameter disk under the same initial conditions are quite different. This is due to the fact that the literature equations are developed for a specific case. Therefore, our own relationship is derived. First, we try to find a relationship between the first wind turbine and its TI_{7D} ($TI(x = 7D)$). At this turbine, the inflow TI corresponds to TI_∞.

The hypothesis made is to assume that the TI_{7D} depends only on a function of C_T at $TI_\infty = 6\%$:

$$TI_{7D} = TI(C_T)|_{TI\infty=6\%} \tag{3.18}$$

Since our model does not calculate TI at any points, we obtain it by interpolating the TI_{7D} from BigFlow simulations (mean in a one diameter disk: MDV) as a function of C_T (Fig. 3.24).

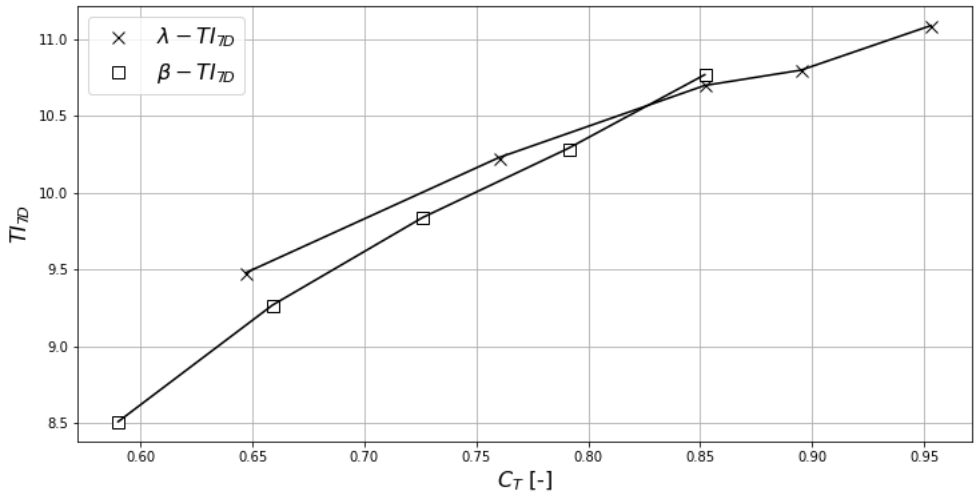

Figure 3.24: Relation between TI_{7D} and C_T (modified with $\beta|_{\lambda=7.55}$ et λ according to Eq. 3.14).

It is important to separate the TI_{7D} obtained by modifying $\beta|_{\lambda=7.55}$ and λ, because their effects on TI_{7D} are not comparable. Indeed, increasing the rotational speed of the rotor creates an angle of attack which varies along the blade. However, changing the pitch produces a change in the angle of attack that is constant. This non-identical behaviour, for the same C_T, causes turbulence intensities that are not equal. By interpolating the result, we obtain the two equations:

$$TI_{7D,\lambda} = -6.52 \cdot C_T^2 + 15.58 \cdot C_T + 2.133 \tag{3.19}$$

$$TI_{7D,\beta} = -9 \cdot C_T^2 + 21.4 \cdot C_T - 0.98 \tag{3.20}$$

The results obtained by our interpolation for the first wind turbine are presented to the Tab. 3.2 & 3.3. The TI_{7D} from BigFlow and the one calculated using our relation Eq. 3.19 & Eq. 3.20 are relatively identical. The literature was used to compare our results with *Lit1* and Lit2 in the next tables corresponding to Eq. 3.15 and Eq. 3.16 respectively, injected in Eq. 3.17 to find TI total. The interpolation of the results is therefore correct. As explained before, there is a significant difference between the literature and the value coming from BigFlow, the interpolation realized gives us more conclusive results. So, we will use it to calculate the TI_{7D}.

At the farm entrance, it can also be seen that the initial TI of 6%, fixed in the BigFlow solver, is not really identical to this value in reality. The real value of the TI_∞ is ≈ 5.66.

WT_0						
TI_∞ [%]	TSR [-]	C_T [-]	$TI_{7D,BF}$ [%]	$TI_{7D,obtained}$ [%]	$TI_{7D,Lit1}$ [%]	$TI_{7D,Lit2}$ [%]
5.65	5.7	0.647	9.48	9.48	13	11
5.66	7.55	0.852	10.76	10.67	14.3	14.5
5.67	8.86	0.953	11.09	11.05	14.9	16.3

Table 3.2: TI_{7D} obtained by our relation against the BigFlow one of the first wind turbine and by varying λ at $\beta = 0°$.

WT_0						
TI_∞ [%]	Pitch [°]	C_T [-]	$TI_{7D,BF}$ [%]	$TI_{7D,obtained}$ [%]	$TI_{7D,Lit1}$ [%]	$TI_{7D,Lit2}$ [%]
5.65	1	0.791	10.29	10.31	14	13.3
5.66	2	0.726	9.84	9.81	13.6	12
5.67	3	0.659	9.27	9.21	13.1	11

Table 3.3: TI_{7D} obtained by our relation against the BigFlow one of the first wind turbine and by varying β at $\lambda = 7.55$.

It is also interesting to look at what happens in case of reusing this relationship to calculate the TI at a distance of 7D from the second WT (waked inflow), in case of a TSR and a pitch angle of the first WT fixed and respectively equal to 7.55 and 0 [°].

Tab. 3.4 represents the same experience as in Tab. 3.2, but for the second WT at fixed operating points for WT_0. This comparison allows us to see that, for the same TSR of 7.55 (and an almost equivalent C_T) and for a larger input TI, we have a lower TI_{7D} for the second wind turbine than for the first (9.9 % instead of 10.76 %). This shows that it is relatively difficult to determine an extremely accurate relationship to find the TI at 7D.

Therefore, for simplicity and noting that the results obtained are not too far from reality (Tab. 3.4, Tab. 3.5), the equation C_T-TI_{7D} is use again (Eq. 3.19, Eq. 3.20) for the second wind turbine. Again, we can see that the TI_{7D} obtained with our interpolation is better than the one provided by the literature. Therefore, we will use our interpolation to calculate the inflow TI of the whole wind turbine farm.

WT_1						
TI_{in} [%]	TSR [-]	C_T [-]	$TI_{7D,BF}$ [%]	$TI_{7D,obtained}$ [%]	$TI_{7D,Lit1}$ [%]	$TI_{7D,Lit2}$ [%]
10.7	5.7	0.638	9.14	9.42	15.8	14.3
10.7	7.55	0.845	9.9	10.64	16.5	17.2
10.7	8.86	0.939	10.2	11.01	17.4	19.4

Table 3.4: Analysis of the TI_{7D} obtained by varying λ of the second turbine. $\lambda_{WT_1} = 7.55$ and $\beta_{0|1} = 0$ [°]. $U_\infty = 9$ [m/s].

WT_1						
TI_{in} [%]	Pitch [°]	C_T [-]	$TI_{7D,BF}$ [%]	$TI_{7D,obtained}$ [%]	$TI_{7D,Lit1}$ [%]	$TI_{7D,Lit2}$ [%]
10.7	1	0.784	9.74	10.26	16.6	16.2
10.7	2	0.718	9.48	9.75	16.3	15.26
10.7	3	0.651	9.27	9.13	11.8	14.5

Table 3.5: Analysis of the TI_{7D} obtained by varying β of the second turbine. $\lambda_{WT_{0|1}} = 7.55$ and $\beta_0 = 0$ [°]. $U_\infty = 9$ [m/s].

Now that all the necessary components for the Shapiro model are set up, we can move on to the superposition model to perform the wakes of the whole farm.

3.5 Extension of the model for three wind turbines in a row

Now that the Shapiro model has been investigated, one can use the equations obtained to test the four superposition models. As a reminder the different methods are:

$$Method\,A : U_w(x,y,z) = U_\infty - \sum_i (U_\infty - u_w^i(x,y,z)) \tag{3.21}$$

$$Method\,B : U_w(x,y,z) = U_\infty - \sqrt{\sum_i (U_\infty - u_w^i(x,y,z))^2} \tag{3.22}$$

$$Method\,C : U_w(x,y,z) = U_\infty - \sum_i (u_{in}^i - u_w^i(x,y,z)) \tag{3.23}$$

$$Method\,D : U_w(x,y,z) = U_\infty - \sqrt{\sum_i (u_{in}^i - u_w^i(x,y,z))^2} \tag{3.24}$$

First the wakes obtained for each model are compared with the one obtained with BigFlow (Fig. 3.25). The BigFlow simulation chosen is the one in which we give the value of the inflow wind of the farm equal to 9 [m/s] (and let the controller choose the operating points for the WTs). In order to compare our graph to the BigFlow one, Shapiro model use the same β, λ and so the same C_T, with k^* computed with previous relationships. As can be seen on this graph (Fig. 3.25), the methods from (A) to (D) have a similar deficit from the outflow of the first WT to the inflow of the next. Indeed, the superposition models (by definition) have effects only starting from the second WT.

Although models (A) and (B) are not really relevant in our case, because of the approximation: $u_{in}^i = U_\infty$. We have represented them anyway. In these two models, the velocity deficit only increases (see Fig. 3.25). Indeed, the deficit is constantly evaluated without taking into account the inflow wind speed (it takes U_∞ instead of u_{in}^i to compute the i^{th} deficit). Looking at the recovery rate, we notice that this last is higher for the square method (B) than for the linear method (A). Knowing that these two models are not interesting to calculate an optimum, we will not describe them in more details.

The two methods of interest (the one taking the effective upstream velocity u_{in}^{i}), (C) and (D) also have very different intensity wakes. Although the model (D) seems to give results closer to those of BigFlow, Fig. 3.26 allows comparing them more precisely to the BigFlow curve (in the sense of the MDV).

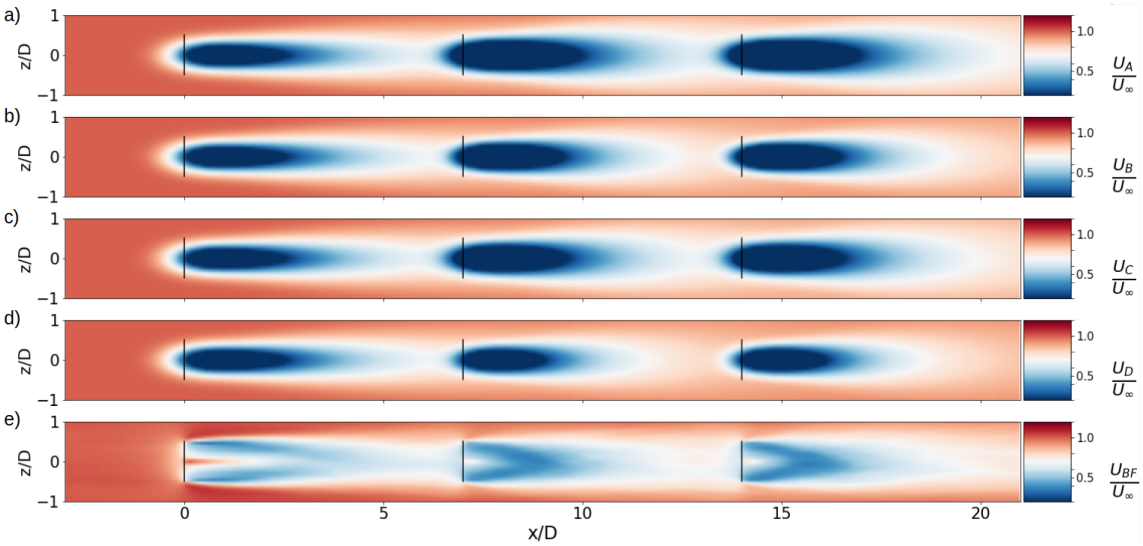

Figure 3.25: Middle-hub wake velocity obtained at $U_\infty = 9$ [m/s] from: (a) Method A (Lissaman 1979), (b) Method B (Katic et al. 1987), (c) Method C (Niayifar Porté-Agel 2016), (d) Method D (Voutsinas et al. 1990), (e) BigFlow.

Comparing the curves with those of BigFlow (Fig. 3.26), we notice that the square superposition model (d) gives better result than the linear one (c). Indeed, we observe that the curve of the linear model does not follow the trend of the BigFlow one. This is mainly due to a velocity drop in the near wake not corresponding to that of BigFlow, which does not allow a similar behaviour. Although the curves of the square model are relatively proper, the wind intensities of the inflow and outflow for the third turbine are not the best. The calibrated expansion coefficient does not give conclusive results. It is too high, creating a widening graph (velocity is varying between more and more extreme velocity values).

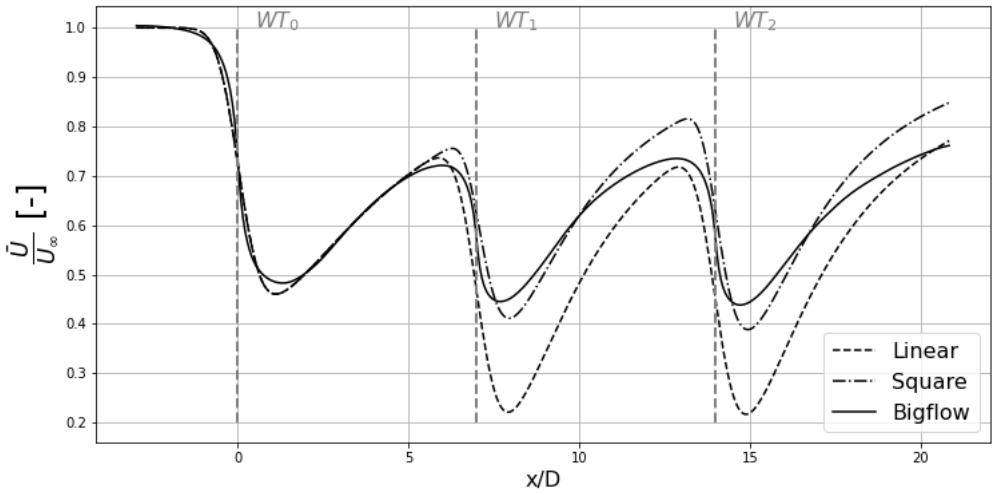

Figure 3.26: MDV: Mean disk velocity of model (c) (Niayifar Porté-Agel 2016) and (d) (Voutsinas et al. 1990) and the BigFlow one. $U_\infty = 9$ [m/s].

Therefore, in view of the previous results, our analysis will focus on the square model (d). Seeing that the k^* is too large, we can look at what happens if the multiplicative factor TI_{factor} is removed in the computation of the k^*. This instinct comes from the fact that the TI_{factor} is a multiplicative factor which, for the last two wind turbines is greater than one which increases too much the value of k^*.

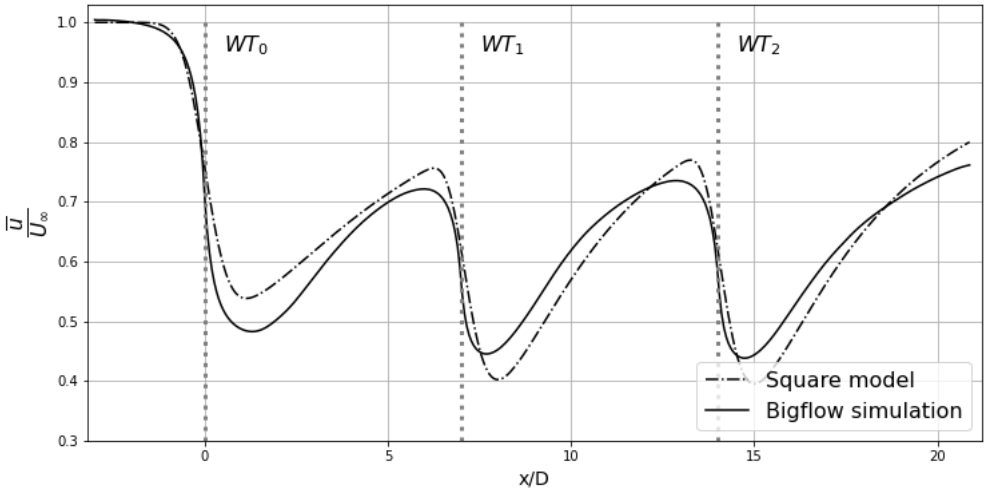

Figure 3.27: MDV: Square model without taking into account the TI_{factor}. $U_\infty = 9$ [m/s].

When comparing the results obtained by removing the TI factor for the last two WT, we realize that they are better than when using this factor. One can check that this result is valid for other values of β and λ on each WT (appendix B.2). Since the wake of the third wind turbine has no impact on the behaviour of the following turbines and their power, we analyse different cases by varying the pitch β and the TSR λ of the first two. We notice by analysing the graphs in the appendix B.2 that the graphs on the right (those without the TI factor) obtain better results than those on the left (those taking into account the TI variation) for all the studied cases (the C_T used for these graphs are those that our BEM computes, it will be explained in the section 3.6).

Seeing this, our final wake model will be obtained using the square superposition model with the calculation of the k^* without the TI_{factor} for the last two turbine Eq. 3.16:

$$k^* = (0.1031 \cdot C_T^3 + 0.0242 \cdot C_T^2 + 0.0144 \cdot C_T + 0.0132)$$

To finalize the farm model, we just have to find a way to compute the C_T. Indeed, until now, for our analysis we used the C_T of BigFlow. In order to have an independent design, a way to compute this C_T must be implemented. It is in this context that the BEM is used.

3.6 Insertion of the BEM in the model

In order to obtain practical values for our model as the C_T, a BEM implementation is used. In section2.2, we see that local velocities along the blades are used to compute these forces. With the development of a wind farm (multiple WTs), we notice that the assumption of a uniform inflow (UI) velocity (normal component velocity into the BEM algorithm) is no longer verified for the waked inflows.

Therefore, in addition to the amplitude, the shape of the wake is still important 7D downstream the WT. We notice high similarity of velocity deficit profiles - 7D downstream of the WT - between Shapiro and BigFlow, in the section 3.3.2. This deficit is shown in Fig. 3.28. In case of Non Uniform Inflow (NUI), we decide to enter the two-dimensional velocity profile of the flow, i.e.

the local velocity that is a function of (y, z), as an input of the NUI BEM.

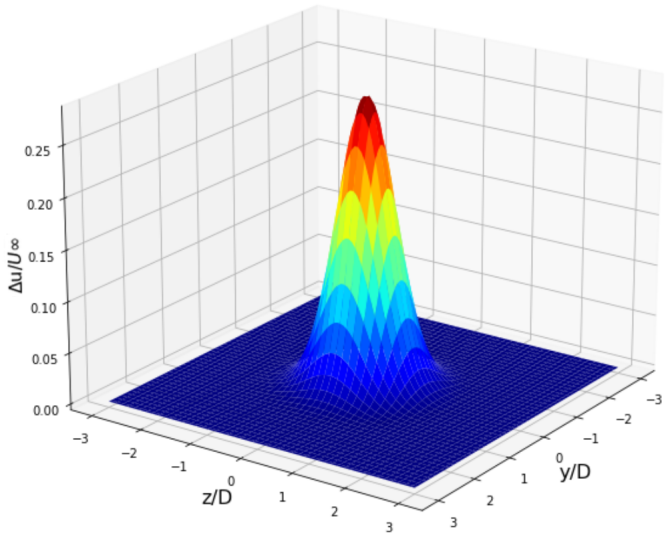

Figure 3.28: Normalized velocity deficit 7D downstream the WT - Shapiro model for $U_\infty = 9$ [m/s] and TSR=7.55.

In case of UI BEM algorithm, the MDV at the position of the WT : x = 7D is computed. This mean velocity is introduced as a single value in the BEM, regarding a uniform freestream velocity for the next WT. For the NUI BEM algorithm, these local velocity deficits is taken into account. The lowest velocity is at the centre of the wake and the velocity increases as the radius of the blade increase. If a disk is considered, it means that this one is lightly loaded at the centre, and highly loaded at the disk ends.

In Fig. 3.29, we compare the thrust and torque of the first and second wind turbine (the third having a similar behaviour as the second) as a function of β and λ. For the first wind turbine, since the inflow wind has a constant distribution along the blade, there is no difference between the UI and NUI BEM (this is the reason why only one BEM curve appears for the left figures).

For all the graphs, the curves are relatively analogous in behaviour but not necessarily in amplitude. We will see later that for the power this does not matter much. We can also spot that for the second wind turbine, the UI BEM is higher in amplitude than the NUI BEM for all graphs, and closer to that of BigFlow. However, we will use the NUI BEM since it is more pragmatic, and since the behaviours are similar and that the amplitudes are not much better.

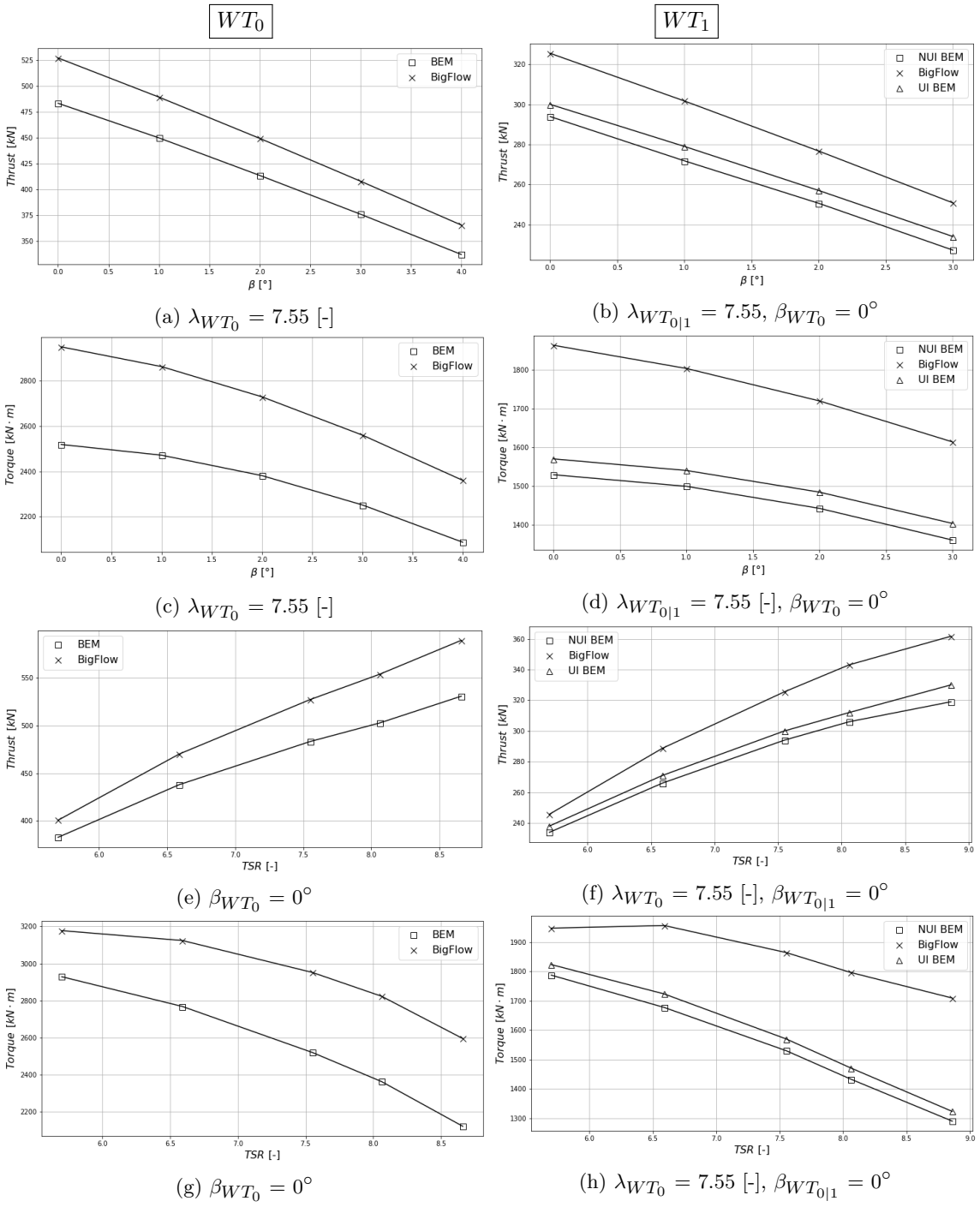

(a) $\lambda_{WT_0} = 7.55$ [-]

(b) $\lambda_{WT_{0|1}} = 7.55$, $\beta_{WT_0} = 0°$

(c) $\lambda_{WT_0} = 7.55$ [-]

(d) $\lambda_{WT_{0|1}} = 7.55$ [-], $\beta_{WT_0} = 0°$

(e) $\beta_{WT_0} = 0°$

(f) $\lambda_{WT_0} = 7.55$ [-], $\beta_{WT_{0|1}} = 0°$

(g) $\beta_{WT_0} = 0°$

(h) $\lambda_{WT_0} = 7.55$ [-], $\beta_{WT_{0|1}} = 0°$

Figure 3.29: Analyse of the thrust and torque for the first and second wind turbine with the NUI BEM, UIBEM and BigFlow by varying either β or λ. $U_\infty = 9$ [m/s].

With the BEM, we have all the necessary components for our final model. Since we have already analysed it for 9 [m/s], it is interesting to see how it behaves for higher wind speeds.

3.7 Application to various freestream velocities

To test our model, we try to compare it to simulations at various freestream velocity. The graphs Fig. 3.30 represent variations in the inflow speed of the farm with the BigFlow controller activated. This means that the only given information is the inflow wind speed, the other parameters are calculated by BigFlow. If our interpolation is used to compute λ and β (as explained in the section: 2.4), the results in Fig. 3.30 are achieved.

The implementation made gives relatively good results when the inflow wind speed of the farm change. However, when we reach 14 [m/s], the intensity of the outflow of the third wind turbine is not excellent. If the computation of the maximum power was wanted, this bad behaviour behind the third wind turbine would not be a problem since it is the last one. To be able to optimize the power for another inflow speed (than 9 [m/s]), we would have to vary the λ and the β to verify that the behaviour is still good. This will not be realized in this research.

It is also interesting to note that, for example, for wind speeds of 12-16 [m/s], for the first WT, the recovery rate is very low. The turbulence created is not sufficient to allow the mixing of the flow at high freestream velocity.

Knowing that our expansion coefficient is limited (slope of the MDV at least zero - no recovery), when our velocity drop is underestimated compared to that of BigFlow, our expansion coefficient can't recover the wind velocity of BigFlow at 7D. This shows us the importance of the velocity drop in the near wake when the recovery rate is low.

The recovery rate of the first wind turbine also changes very strongly between freestream velocity 10 and 12 [m/s]. Despite this big change in behaviour, we notice that the k^* follows this trend and gives good results. Since our model is calibrated and gives good outcomes, we can use it to optimize the power of our farm. This is the subject of the next section.

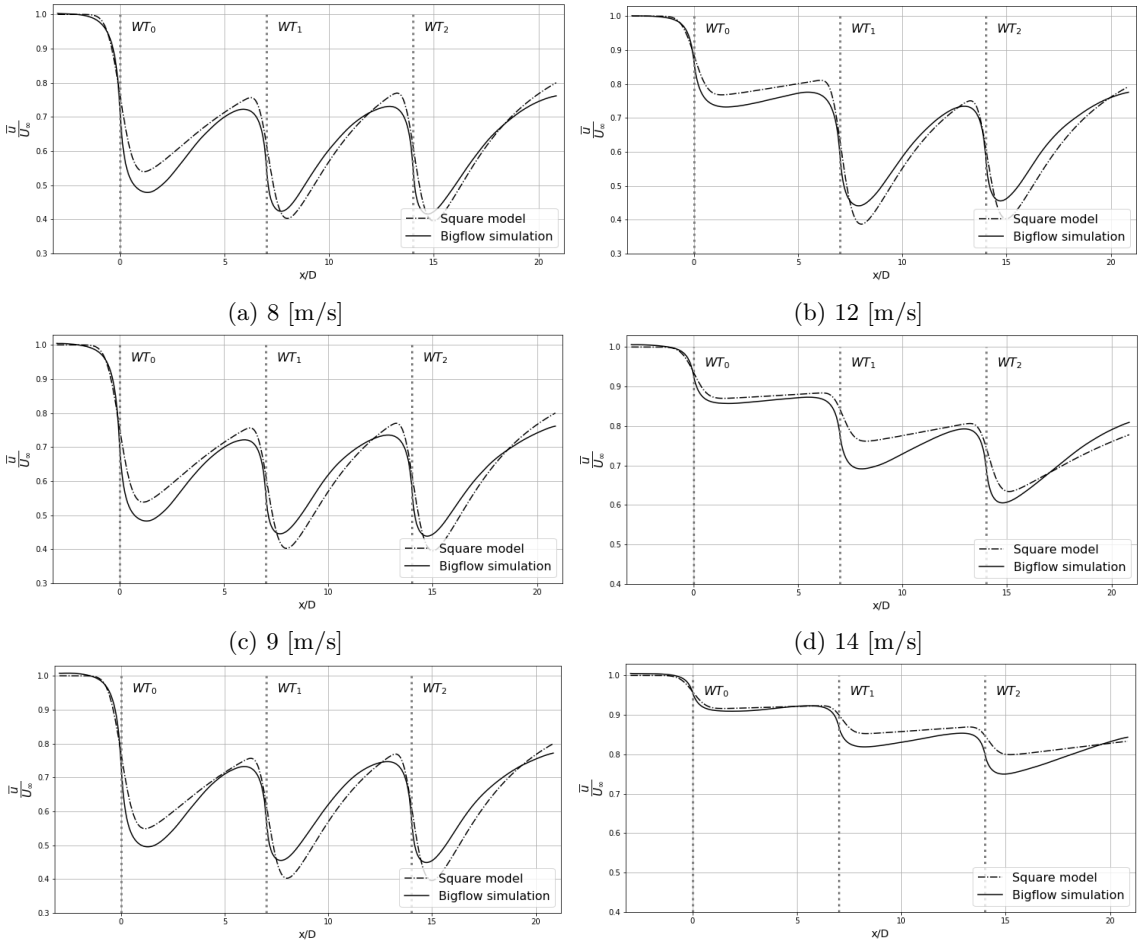

(a) 8 [m/s]

(b) 12 [m/s]

(c) 9 [m/s]

(d) 14 [m/s]

(e) 10 [m/s]

(f) 16 [m/s]

Figure 3.30: MDV: BigFlow simulations and the implemented model for several inflow wind of the farm.

Chapter 4

Application case : Total power optimization

In this following chapter, the power that our model provides (using the torque supplied by the BEM) is compared to that of BigFlow. The objective is to verify that our model can exploit it to optimize the farm. Then, we use this power to find the optimum of our farm according to the rotor speed and the pitch angle of each wind turbine.

4.1 BEM power analysis

In this section, we compare the power of BigFlow and BEM by varying the λ and β for the first and the second wind turbine (as we do in Fig. 3.29, section:3.6). As a reminder, the mechanical power of the second wind turbine is based on $\lambda_{WT_0} = 7.55$ and $\beta_{WT_0} = 0$ [°].

In Fig. 4.2, the first observation to make is that the values in amplitude of the power do not correspond. Although it does not match, to find a maximum, it is not necessary to have the real power values, as long as this optimization gives us the right optimum. Once the latter is found, we just need to enter the β and λ values of each wind turbine (provided by the optimization) in BigFlow to get the effective mechanical power. For this, the behaviour of the curves must correspond.

As the BigFlow controller is not activated (i.e. change in rotational speed of the rotor & pitch angle), we realize that the graphs of power-λ does not reach a maximum for BigFlow power. In fact, once the controller is activated, it optimizes the power of the wind turbine by following the maximum provided by the curve realized by the Maximum Power Point Tracker (MPPT) technique. To obtain this curve using this technique, the experiment consists of varying the rotor speed at a fixed free-flow speed, and obtaining the maximum power. Then, the obtained maximum power point belongs to the curve. The experiment is repeated to determine all the maximum power points at different freestream velocities. All these maximums will define the curve using the MPPT method, as shown in Fig. 4.1.

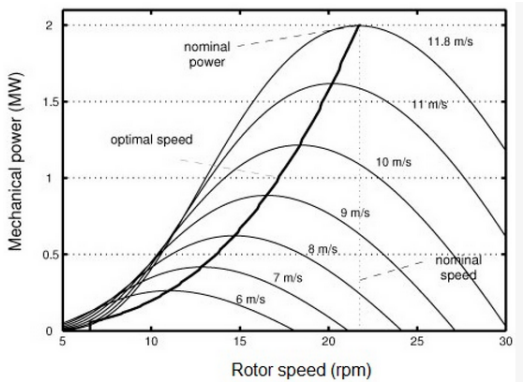

Figure 4.1: Representation of Maximum Power Point Tracking control (MPPT) according to the rotor speed for severals inflow wind speed [18](Ramadoni Syahputra, Indah Soesanti).

The MPPT curves behave similarly to the outcomes we observe by using our BEM model presented in Fig. 4.2a. It is easy to verify that the optimum found by our model is close to that of BigFlow with active controller by analysing the value of the rotor speed found by BigFlow for the first wind turbine. For a wind turbine with an inflow of 9 [m/s], the rotor speed provided by the BigFlow controller gives us: TSR $\approx$ 8.04 at given rotor speed = 10.97 [rpm], and we get a value with our model : TSR $\approx$ 8 giving a rotor speed = 10.91 [rpm].

In the BigFlow simulation, the second wind turbine also fits its rotor speed on its perceived wind inflow. This is the reason why, for the second wind turbine (Fig. 4.2b), the optimum found (calculated on the real inflow wind of the wind turbine) give $\lambda \approx 8$ and rotor speed = 8.6 [rpm] and for BigFlow with controller: $\lambda = 8.19$ and rotor speed = 8.82 [rpm].

Thus, the optimum reached corresponds relatively well to that of BigFlow. Therefore, the power provided by our BEM is relevant to optimimize the farm. The values obtained after our optimization will, in any case, be checked prospectively.

Finding the optimum power according to various pitch angles is easier. Indeed, it corresponds to the value $\beta = 0$ in stand-alone condition. As the pitch increases, the power decreases and the curve of BigFlow and our BEM have similar trends in both cases WT_0 (Fig. 4.2c) and WT_1 (Fig. 4.2d)

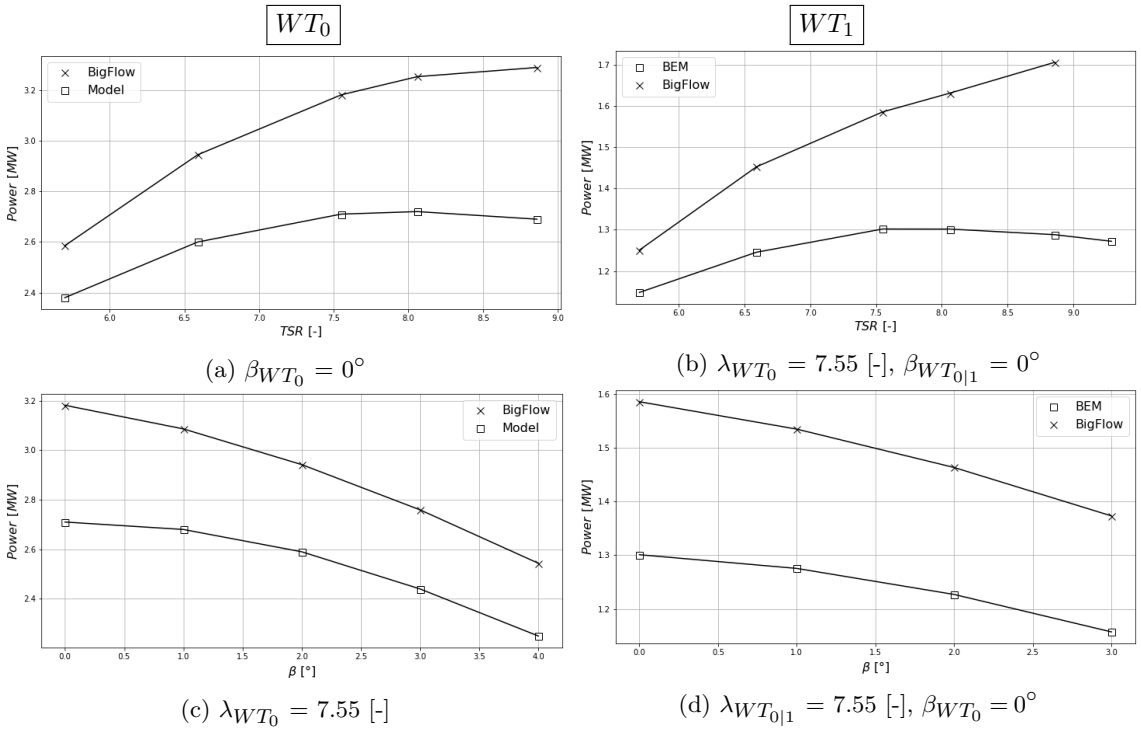

(a) $\beta_{WT_0} = 0°$

(b) $\lambda_{WT_0} = 7.55$ [-], $\beta_{WT_{0|1}} = 0°$

(c) $\lambda_{WT_0} = 7.55$ [-]

(d) $\lambda_{WT_{0|1}} = 7.55$ [-], $\beta_{WT_0} = 0°$

Figure 4.2: Power of BigFlow solver and NUI BEM by varying either λ or β for the two first turbines. $U_\infty = 9$ [m/s].

Since the NUI BEM give us relatively conclusive results, one can verify if it is possible to find an optimum by controlling λ and β.

4.2 Optimization strategy

From this section, only the model covered in the last part is considered. Power and thrust coefficient come from the model, if it is not specified.

In this research, the control strategy used is referred as *axial-induction-based control*. The axial induction is related to the thrust coefficient in our model as $a = \frac{1}{2}\left(1 - \sqrt{1 - C_T}\right)$, thanks to momentum theory, developed in section 2.2. As already mentioned, the upstream turbines induce a velocity deficit for the inflow to the downstream WT. The strategy consists to control either the pitch or the rotor speed to reduce the axial induction of an upstream turbine to allow the wind to reach a higher speed for a downstream turbine and increase the overall energy extraction.

In momentum theory, the optimum induction factor ($a_{opt} = 1/3$) corresponds to the optimum power coefficent ($C_{p,opt} = 16/27$ [7]), as we can see on Fig. 4.3. At a_{opt}, the power coefficient is not really sensitive to a slight variation in the induction factor, but the thrust coefficient is. The idea is to lower the optimal induction factor, such that the thrust coefficient decreases, enabling higher speed downstream, without drastically changing the extracted power.

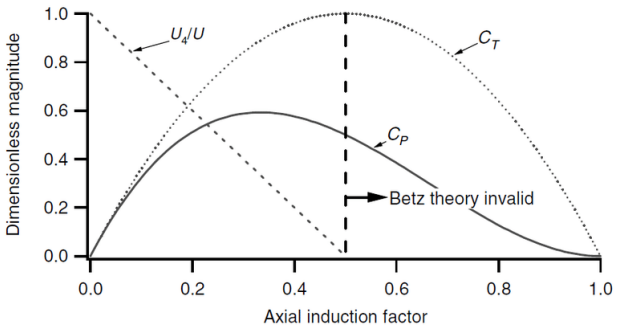

Figure 4.3: Power and thrust coeffictient curve according to the axial induction coefficient from momentum thory. [7].

The diagram illustrated in Fig. 4.4 represent the methodology used to achieve an axial induction-based control strategy. In order to find an optimal value for the total power of the wind farm, we change either the pitch or the rotor speed of the first two turbines and compute the total power of the farm. Indeed, the last one only has to maximize its own power since there is no wind turbine behind it (with β and ω interpolated tanks to BigFlow simulations, as explained in section 2.4). When an optimal value for the total farm power is found, the corresponding rotor speed and pitch angle of each turbine are recorded and transmitted to BigFlow to obtain the actual power. It is interesting to note that block 1 in Fig. 2.6 has been removed (in Fig. 4.4) since β and ω (for the first two turbines) are now model parameters. This block is only useful for the third wind turbine.

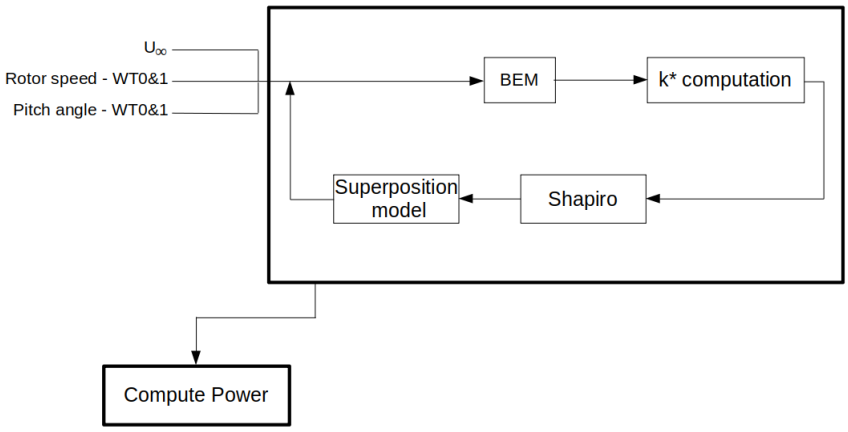

Figure 4.4: Methodology used to perform axial induction control.

4.2.1 Axial induction control using rotor speed

In this section, an analysis of the power behaviour by varying the rotor speed of WT_0 and WT_1 is performed.

On the 3D graph (Fig. 4.5), there is a power optimum of the farm when the rotor speed of the first two wind turbines varies. It can also be seen that when one of the two rotor speed is fixed and that the other change, the obtain curve has an optimum (by slicing the graph, at fixed ω_0 / $\omega 1$). This enables us to see that no matter what the ω value of one of the two wind turbines is, the other always has only one possible rotor speed to reach the maximum. Therefore, there is only one couple $[\omega_1, \omega_2]$ that allows maximizing the farm.

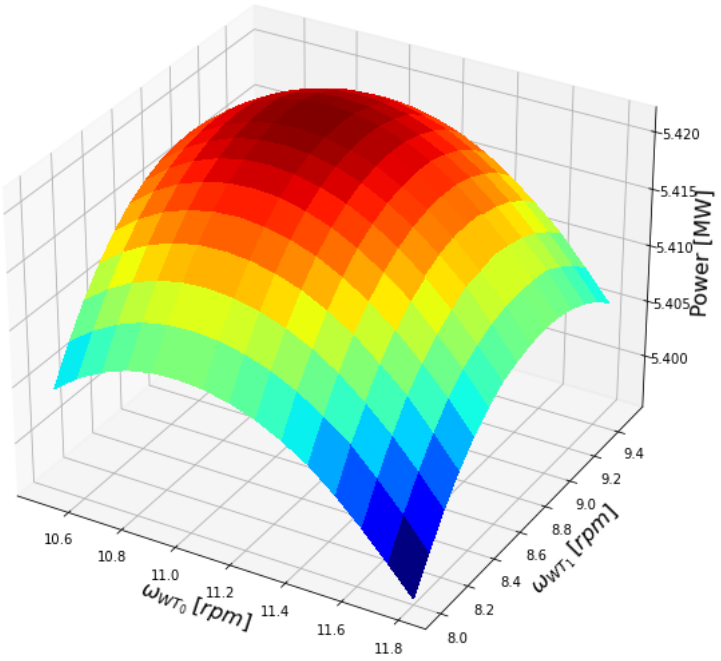

Figure 4.5: Total mechanical power of the farm for various rotor speed - $U_\infty = 9$ [m/s].

By putting the couple we found [ω_1, ω_2] in BigFlow solver and calculating the power corresponding to each of the wind turbine, we get the result in Tab. 4.1. The total power of the farm is equal to 6.514 [MW] (the sum of the power of each turbine).

	Rotor Speed [rpm]	Pitch [°]	Power [MW]
WT_0	10.96	0	3.250
WT_1	8.96	0	1.623
WT_2	8.66	0	1.641

Table 4.1: Power computation by BigFlow solver at the optimum found ($\omega_{0,opt}$, $\omega_{1,opt}$ using axial based control induction).

By optimizing each wind turbine independently, a similar result to the one obtained when maximizing the total power of the farm is got. Individual optimization is done by incrementally optimizing the wind turbines considering the wind they receive. Thus, the inflow of each wind turbine depends on the prior optimization of the previous turbine(s).

This shows that the optimization is not conclusive, since this type of control does not allow a higher power output than turbine-by-turbine optimization. This result can be explained: changing the TSR of a wind turbine does not greatly affect the inflow wind of the next, as shown in Fig. 4.7. This is explained in the Fig. 4.6 (inspired by the article [22]). Indeed, the aim is to decrease the rotor speed in order to have a higher flow (at least not too slowed down) for the next one. This means accepting that the upstream wind turbine produces a little less to allow the following ones to produce more. Decreasing the rotor speed creates less turbulence and therefore a lower recovery after it. In the end, this will not have a big impact on the wind intensity of the next turbine. Therefore, the power lost by the upstream turbine is not counterbalanced by a possible gain in power of the downstream turbine(s).

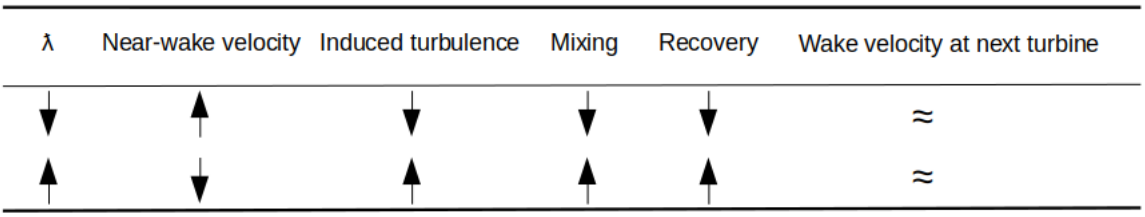

Figure 4.6: Causal relations due to a change in λ.

The impossibility of induction control leading to higher-power production at this distance is confirmed in paper [22]. In this paper, they use the same spacing, but with different turbines than ours. Indeed, they found that the induction control did not offer better results than an individual optimization of the wind turbines.

To verify our outcome, one can verify what large changes in λ imply on the wind intensity inflow of the following wind turbine. To do so, we can check the behaviour of the curves with BigFlow (Fig. 4.7). On these curves the behaviour explained in Fig. 4.6 can be recognized. Significant variations in TSR have little influence on the inflow of the next wind turbine. This allows confirming our previous results.

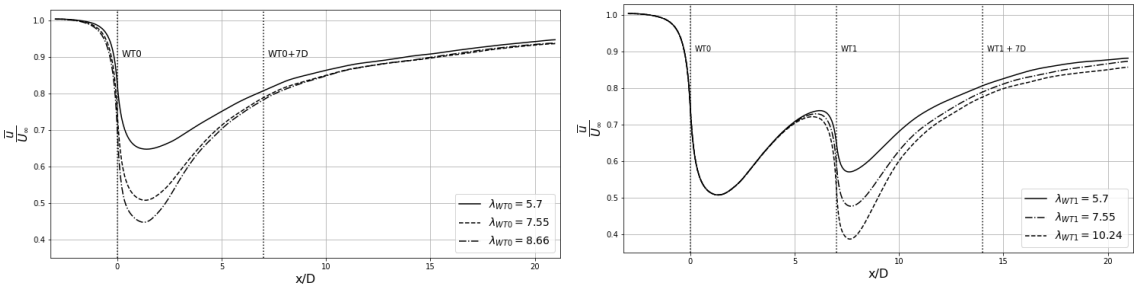

(a) $\beta_{WT_0} = 0°$ (b) $\lambda_{WT_0} = 7.55$ [-], $\beta_{WT_{0|1}} = 0°$

Figure 4.7: MDV: Influence of a change of (a) λ_{WT0} (b) λ_{WT1} on the next wind turbine inflow. $U_\infty = 9$ [m/s].

Power comparison to BigFlow

Knowing that the result gotten is the optimization of each wind turbine individually, it is expected that BigFlow's power to be better than ours. In fact, BigFlow also optimizes the power of each wind turbine individually, but is necessarily more accurate than our model. Indeed, this is confirmed by observing the power obtained with the value of BigFlow $P_{BF} = 6.538$ [MW] (Tab.4.2), (+0.024 [MW] compared to our optimization). This comes from the fact that the optimum discovered is not quite the finest. However our model finds an optimum which is really close to the BigFlow one.

	Rotor Speed [rpm]	Pitch [°]	Power [MW]
WT_0	10.97	0	3.258
WT_1	8.82	0	1.604
WT_2	8.909	0	1.676

Table 4.2: BigFlow rotor speed and power calculated by BigFlow controller.

Now, one can move on to the axial induction control using pitch angle to see if the same results are observed.

4.2.2 Axial induction control using pitch angle

Analysing the graph in Fig. 4.8 gives an optimum power when the pitch angle of each WT is equivalent to 0 [°]. This graph is realized at rotational speed interpolated according to the inflow velocity (as explained in the section: 2.4). As before, this result leads us to the same conclusion. Indeed, not putting a pitch angle means optimizing each wind turbine individually.

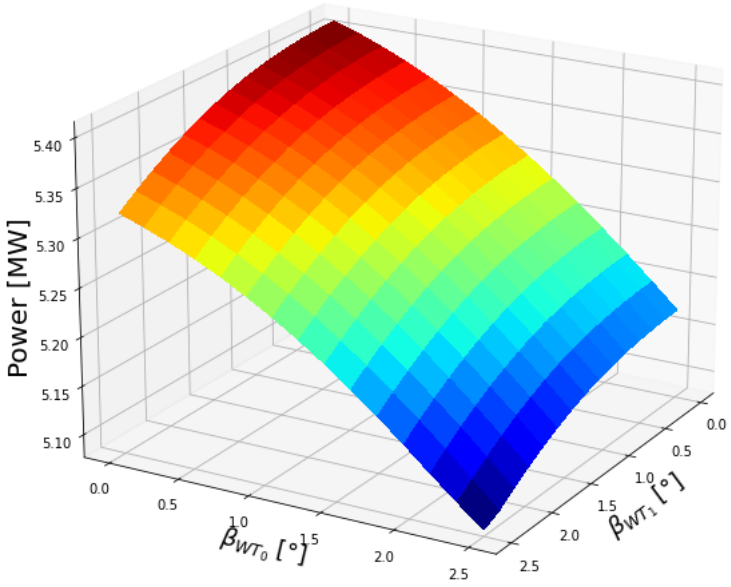

Figure 4.8: Total mechanical power of the farm for various pitch - $U_\infty = 9$ [m/s].

As for the λ, the impact of the pitch angle on a wind turbine has small influence on the inflow wind of the following wind turbine(s). Again, the aim is to see if an increase in β create a larger inflow wind at 7D downstream the turbine. Amplifying this angle on a WT will create less turbulence and produce a weaker recovery outflow. This lower recovery prevents reaching higher inflow velocity for the next turbine. Finally, the inflow of the next wind turbine is slightly impacted (Fig. 4.9).

β	Near-wake velocity	Induced turbulence	Mixing	Recovery	Wake velocity at next turbine
↓	↓	↑	↑	↑	≈
↑	↑	↓	↓	↓	≈

Figure 4.9: Causal relation due to a change in β.

Let us confirm the results obtained with the BigFlows curves by varying β (Fig. 4.10). The curves show us that the power losses caused by an increase in pitch cannot be compensated by the following wind turbine power gains.

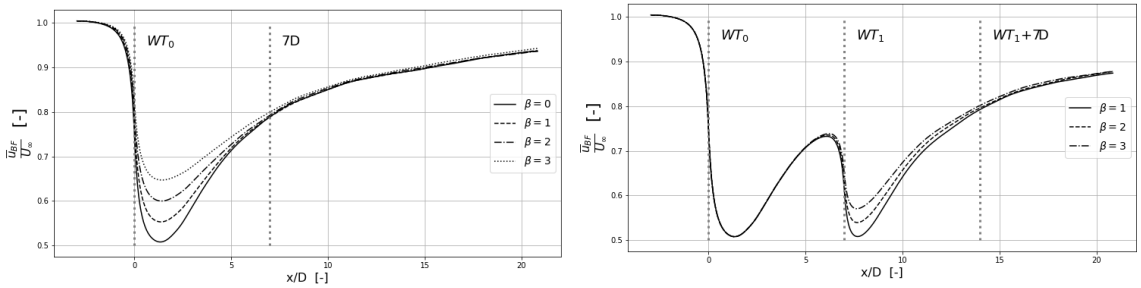

(a) $\lambda_{WT_0} = 7.55$ [-]

(b) $\lambda_{WT_{0|1}} = 7.55$ [-], $\beta_{WT_0} = 0°$

Figure 4.10: MDV: Influence of a change of (a) β_0 (b) β_1 on the next wind turbine inflow. $U_\infty = 9$ [m/s].

Power comparison to BigFlow

Since the optimum found is the one for which the ω are interpolated from BigFlow at $\beta = 0$ [°], this leads to the same power as BigFlow with controller. So the implemented farm did not obtain an improvement of the power. Therefore, the results are the one we get previously (Tab.4.2).

Chapter 5

Conclusions

An isolated wind turbine model was developed and calibrated. By analysing the evolution of the wake with several parameters, a relationship linking the expansion factor to the operating points and conditions was obtained. When our results were compared to those in the literature, it had be seen that our model produced outcomes that were more comparable to those of the LES approach (BigFlow) at various operating points. Then, the isolated wind turbines wake model was extended to the whole farm. To do this, different superposition models were tested and one of them was selected. This choice of the superposition model offered good results but the expansion factor relation found for an isolated turbine had to be adapted for the last two wind turbines. To obtain the thrust coefficient and thus stop depending on BigFlow, a BEM method was used. This last was analysed and compared to BigFlow to verify that it produced good results (in terms of thrust and torque) wich could be used. After checking that the power returned by the BEM had a good optimum power for a consistent pitch angle and rotor speed, we have optimized the power of our farm model.

While trying to optimize our farm using axial induction control, it was seen that the optimum found do not improved the power compared to the power optimization for each individual wind turbine. Indeed, introducing the optimum in BigFlow does not result in a power improvement. These results were confirmed by the literature, in the studied case.

To get a real benefit using axial induction control to optimize the mechanical power, it would be interesting to:

- Test for faster freestream wind speeds. In fact, the recovery rate will be lower at greater freestream velocities. Therefore, the impact of the near-wake velocity drop will be more important. The induction will therefore have a more significant effect on the next wind turbine and thus on the total power of the farm.
- Decrease spacing between turbines. It was found that the pitch angle and the rotor speed do not vary the inflow speed perceived by the next turbine sufficiently. Indeed, the distance between turbines allows to the flow a high recovery. Therefore, decreasing the space between turbines means that the wake "velocity drop" in the near-disk region will have a greater impact, because the recovery does not have enough time to develop.
- Increase the number of turbines in the farm to increase the total energy lost from the wind flow. An axial induction control seems to be more relevant to use in this case.

To perform a power optimization, we could also deflect the wake: this involves turning the nacelle with respect to the actual wind direction. Thanks to the wakes deflection of the upstream turbines, the downstream ones are not totally affected by the wake effects. This approach is called *yawed wind turbine*. Notice that a yaw misalignment indicates that a less proportion of the wind's energy will pass through the rotor area. Thus a single yawed wind turbine typically undergoes a decrease in power production. However, thanks to the deflection of the wake, a real impact on the

overall power output of the farm can be reach.

Finally, knowing that induction control does not improve the power of the farm at 9 [m/s], it can be concluded that, for a freestream velocity below 9 [m/s], this will not be the case either.

Appendices

A.1 Curve analysis with various k^* and C_T

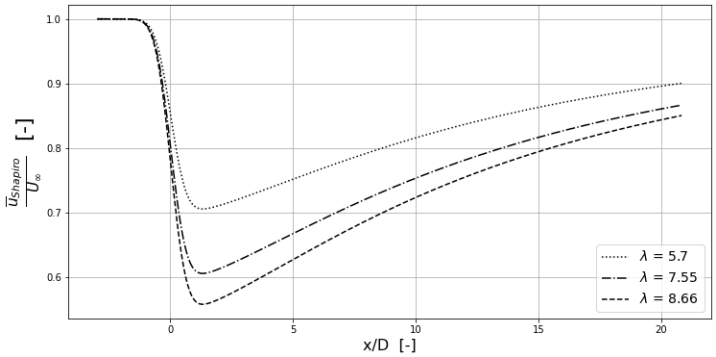

(a) $k^* = 0.04$

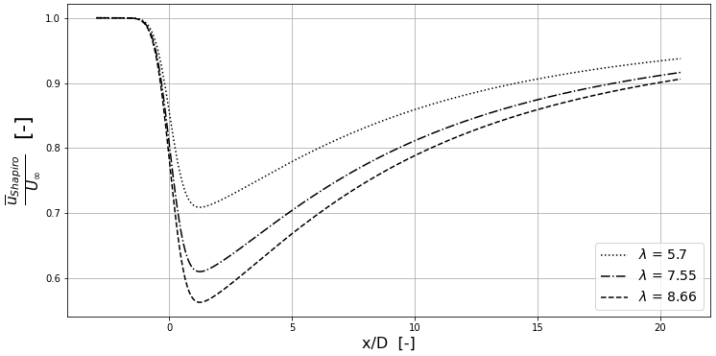

(b) $k^* = 0.06$

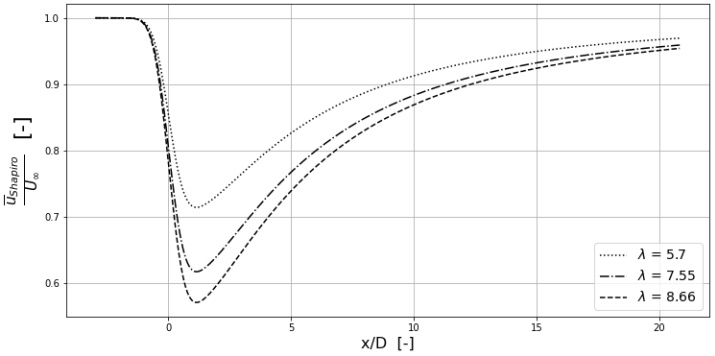

(c) $k^* = 0.1$

Figure 1: MDV: Analysis of the behaviour of mean velocity as a function of λ and k^*. $U_\infty = 9$ [m/s].

B.2 Impact of TI_{factor} on the second wind turbine

With TI_{factor} | **Without TI_{factor}**

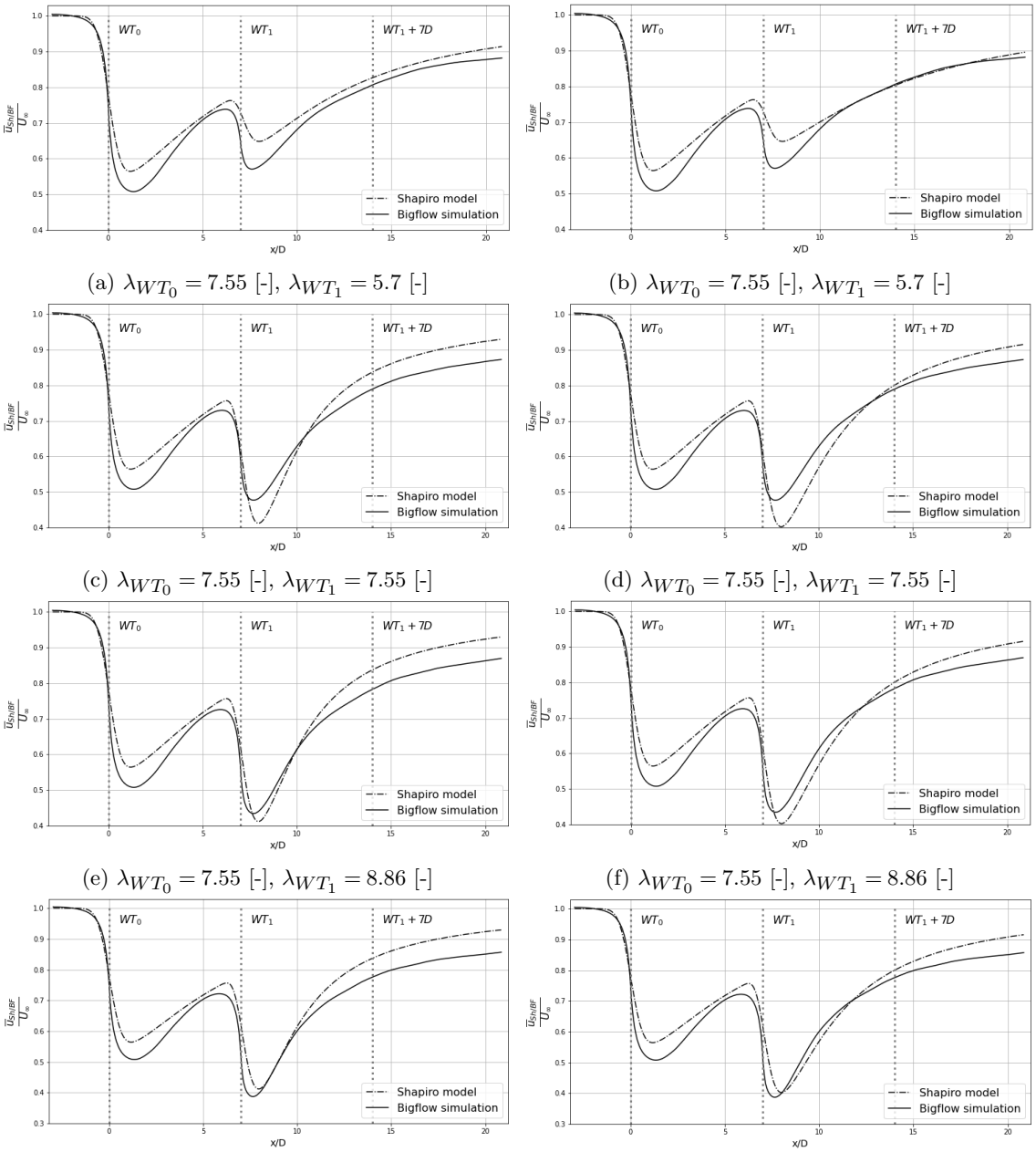

(a) $\lambda_{WT_0} = 7.55$ [-], $\lambda_{WT_1} = 5.7$ [-]

(b) $\lambda_{WT_0} = 7.55$ [-], $\lambda_{WT_1} = 5.7$ [-]

(c) $\lambda_{WT_0} = 7.55$ [-], $\lambda_{WT_1} = 7.55$ [-]

(d) $\lambda_{WT_0} = 7.55$ [-], $\lambda_{WT_1} = 7.55$ [-]

(e) $\lambda_{WT_0} = 7.55$ [-], $\lambda_{WT_1} = 8.86$ [-]

(f) $\lambda_{WT_0} = 7.55$ [-], $\lambda_{WT_1} = 8.86$ [-]

(g) $\lambda_{WT_0} = 7.55$ [-], $\lambda_{WT_1} = 10.24$ [-]

(h) $\lambda_{WT_0} = 7.55$ [-], $\lambda_{WT_1} = 10.24$ [-]

Figure 2: MDV: Comparison between using TI_{factor} or not and by varying the TSR of the second wind turbine.

With TI_{factor} **Without TI_{factor}**

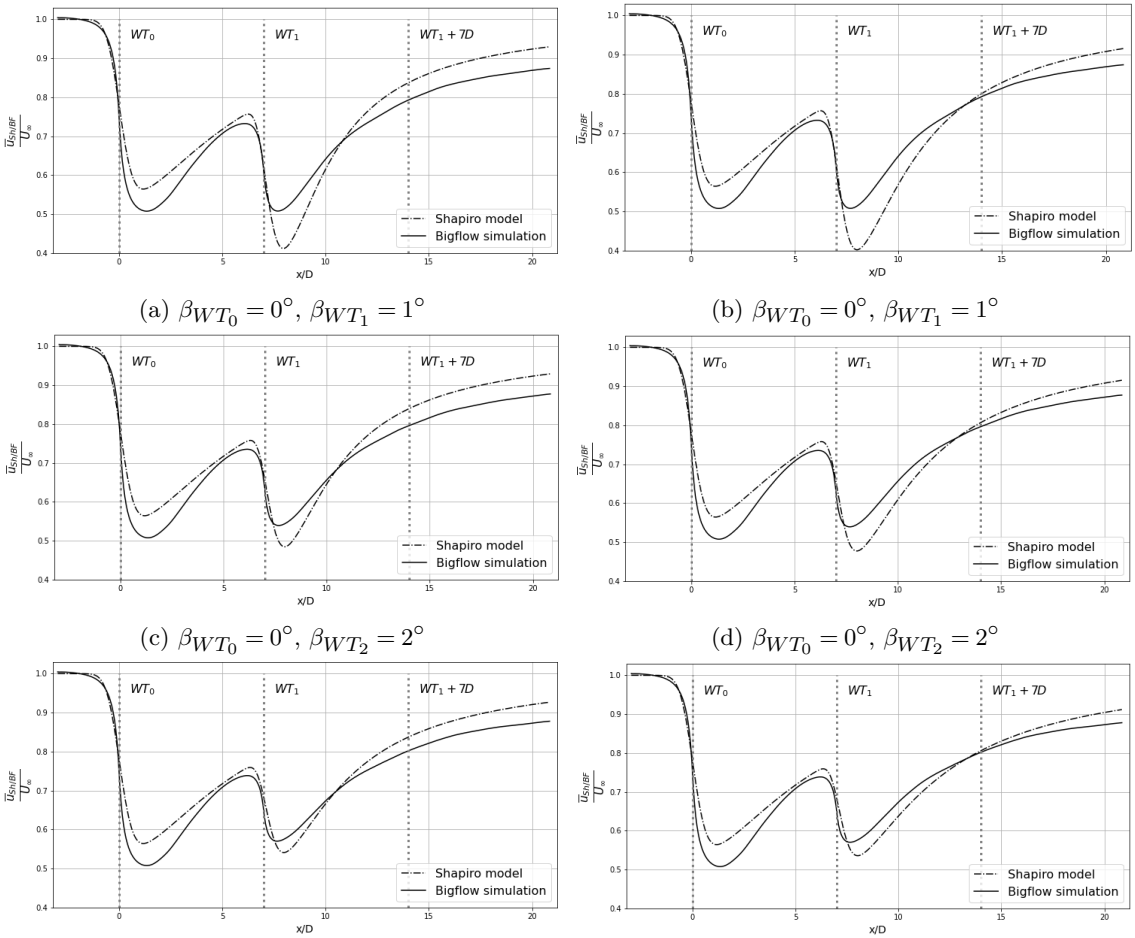

(a) $\beta_{WT_0} = 0°$, $\beta_{WT_1} = 1°$

(b) $\beta_{WT_0} = 0°$, $\beta_{WT_1} = 1°$

(c) $\beta_{WT_0} = 0°$, $\beta_{WT_2} = 2°$

(d) $\beta_{WT_0} = 0°$, $\beta_{WT_2} = 2°$

(e) $\beta_{WT_0} = 0°$, $\beta_{WT_3} = 3°$

(f) $\beta_{WT_0} = 0°$, $\beta_{WT_3} = 3°$

Figure 3: MDV: Comparison between using TI_{factor} or not and by varying the pitch of the second wind turbine at $\lambda_{WT_0|WT_1} = 7.55$.

Bibliography

[1] Advantages and challenges of wind energy. https://www.energy.gov/eere/wind/advantages-and-challenges-wind-energy. [Online; accessed 13-08-2022].

[2] Burning of fossil fuels. https://ugc.berkeley.edu/background-content/burning-of-fossil-fuels/. [Online; accessed 13-08-2022].

[3] Sources of greenhouse gas emissions - epa. https://www.epa.gov/ghgemissions/sources-greenhouse-gas-emissions#:~:text=The%20largest%20source%20of%20greenhouse,Greenhouse%20Gas%20Emissions%20and%20Sinks. [Online; accessed 13-08-2022].

[4] F. Porté-Agel A. Niayifar. *Analytical modeling of wind farms: a new approach for power prediction.* Frede Blaabjerg, 2016.

[5] Not Specified author. Aerodynamics performance, momentum theory. *University of Notre Dame*, N.D.

[6] L. Bricteux. *Simulation of turbulent aircraft wake vortex flows and their impact on the signals returned by a coherent Doppler LIDAR system.* PhD thesis, Université Catholique de Louvain, 2008.

[7] B. DOSE. Cfd simulations of a 2.5 mw wind turbine using ansys cfx and openfoam. Master's thesis, University of Applied Science Kiel, 2013.

[8] M. Duponcheel. *Direct and large-eddy simulation of turbulent wall-bounded flows: further development of a parallel solver, improvement ofmultiscale subgrid models and investigation of vortex pairs in ground effect.* PhD thesis, Université Catholique de Louvain, 2009.

[9] L. Georges. *Development and validation of a LES methodology forcomplex wall-bounded flows. Application to high order structured and industrial unstructured solvers.* PhD thesis, Université Catholique de Louvain, 2007.

[10] N.O. Jensen I. Katic, J. Højstrup. A simple model for cluster efficiency. in european wind energy association conference and exhibition. 1987.

[11] W. Musial J. Jonkman, S. Butterfield and G. Scott. *Definition of a 5-MW Reference Wind Turbine for Offshore System Development, Technical Report TP-500-38060.* NREL, February 2009.

[12] N.O. Jensen. A note on wind generator interaction. *Risø National Laboratory*, 1983.

[13] M. Ge Q. Zhang Li Li, Z. Huang. A novel three-dimensional analytical model of the added streamwise turbulence intensity for wind-turbine wakes. *Elsevier*, 2021.

[14] P.B.S. Lissaman. *Energy effectiveness of arbitrary arrays of wind turbines.* J. Energy, 1979.

[15] F. Porté-Agel M. Bastankhah. A new analytical model for wind-turbine wakes. *École Polytechnique Fédérale de Lausanne*, 2013.

[16] J. Mann. *Probabilistic Engineering Mechanics*, volume 13(4): 269 - 282, chapter Wind field simulation. Elsevier Science Ltd, 1998.

[17] M. Moens. *Large eddy simulation of wind farm flows: improved Actuator Disk model and investigations of wake phenomena.* PhD thesis, Université Catholique de Louvain, 2018.

[18] I. Soesanti R Syahputra. Performance improvement for small-scale wind turbine system based on maximum power point tracking control. *Energies 2019*, 2019.

[19] H. Ritchie and M. Roser. Emissions by sector. *Our World in Data*, 2020.

[20] K. Rados A. Zervos S. Voutsinas. *On the analysis of wake effects in wind parks.* Sage Publications, Ltd, 1990.

[21] P. Nielsen T. Sørensen, M. Lybech Thøgersen. Adapting and calibration of existing wake models to meet the conditions inside offshore wind farms. Technical report, EMD International A/S, 2008.

[22] J. Annoni *et al.* Analysis of axial-induction-based wind plant control using an engineering and a high-order wind plant model. *University of Minnesota*, N.D.

[23] Shapiro *et al.* Modelling yawed wind turbine wakes: a lifting line approach. *Johns Hopkins University*, 2018.

[24] H. Zong and F. Porté-Agel. A momentum-conserving wake superposition method for wind farm power prediction. *Cambridge University Press*, 2019.

UNIVERSITÉ CATHOLIQUE DE LOUVAIN
École polytechnique de Louvain
Rue Archimède, 1 bte L6.11.01, 1348 Louvain-la-Neuve, Belgique | **www.uclouvain.be/epl**